

RESEARCH ARTICLE

Calcium waves facilitate and coordinate the contraction of endfeet actin stress fibers in *Drosophila* interommatidial cells

Donald F. Ready and Henry C. Chang*

ABSTRACT

Actomyosin contraction shapes the *Drosophila* eye's panoramic view. The convex curvature of the retinal epithelium, organized in ~800 close-packed ommatidia, depends upon a fourfold condensation of the retinal floor mediated by contraction of actin stress fibers in the endfeet of interommatidial cells (IOCs). How these tensile forces are coordinated is not known. Here, we discover a previously unobserved phenomenon: Ca^{2+} waves regularly propagate across the IOC network in pupal and adult eyes. Genetic evidence demonstrates that IOC waves are independent of phototransduction, but require the inositol 1,4,5-triphosphate receptor (IP3R), suggesting that these waves are mediated by Ca^{2+} releases from endoplasmic reticulum stores. Removal of *IP3R* disrupts stress fibers in IOC endfeet and increases the basal retinal surface by ~40%, linking IOC waves to facilitation of stress fiber contraction and floor morphogenesis. Furthermore, *IP3R* loss disrupts the organization of a collagen IV network underneath the IOC endfeet, implicating the extracellular matrix and its interaction with stress fibers in eye morphogenesis. We propose that coordinated cytosolic Ca^{2+} increases in IOC waves promote stress fiber contractions, ensuring an organized application of the planar tensile forces that condense the retinal floor.

This article has an associated 'The people behind the papers' interview.

KEY WORDS: *Drosophila*, Actomyosin contraction, Calcium waves, Eye

INTRODUCTION

Tissue construction during development often requires a specific subset of its constituent cells to undergo orchestrated shape change. To accomplish this, tensile forces from actomyosin networks, which are crucial for maintaining and regulating cell shapes, need to be spatially and temporally coordinated in a selective cell population (Guillot and Lecuit, 2013; Paluch and Heisenberg, 2009; Heisenberg and Bellaïche, 2013). Although the mechanism behind the actomyosin contraction *in vitro* and in individual cells has been extensively studied, how these forces are coordinated across a cell field during tissue formation is not well understood.

To investigate the mechanisms coordinating the contractile forces required for tissue morphogenesis, we have used the *Drosophila* compound eye, a convex epithelium with stereotypical

cell composition and arrangement (Waddington, 1962). The compound eye consists of ~800 unit eyes, termed ommatidia, each comprising a distal corneal lens secreted by four cells and two primary pigment cells positioned above eight photoreceptors elongated on the optical axis. Ommatidia are embedded in a honeycomb lattice of interommatidial cells (IOCs), pigment-secreting cells that separate and optically insulate ommatidia. At the retinal floor, IOCs flatten their endfeet to form the fenestrated membrane, an extracellular matrix (ECM)/cytoskeletal specialization that defines the proximal surface of the eye (Fig. 1). The ECM specializations include grommets, the circular openings that allow photoreceptor axons to exit the retina, and ridges, the dense linear ECM between neighboring grommets. This reiterative nature of the eye architecture implies the tensile forces for cell morphogenesis in one cluster are similarly applied in all other ommatidia across the retina, making the eye uniquely suited for analyzing how local forces are coordinated to ensure proper tissue formation.

Actomyosin-dependent contraction has been implicated in several processes during fly eye development, including apical cell constriction in the morphogenetic furrow (MF; an indentation that sweeps across the larval eye disc) (Benlali et al., 2000; Fernandes et al., 2014), pigment cell shape and photoreceptor position in the epithelium (Warner and Longmore, 2009a; Warner and Longmore, 2009b; Lee and Treisman, 2004), rhabdomere biogenesis (Baumann, 2004; Galy et al., 2011) and retinal lumen formation (Nie et al., 2014). In addition, actomyosin tensile forces participate in the reduction of retinal basement, a process that is essential for the formation of the curvature of the eye. During the latter half of pupal development, the IOC endfeet undergo a fourfold contraction (Longley and Ready, 1995), shaping the ommatidia into elongated hexagonal prisms that become packed to give the eye its panoramic convex curvature (Fig. 1B). Planar tension at the retinal floor has the additional role of aligning the rhabdomeres, photosensory waveguides, of each ommatidium along the optical axis. Rhabdomeres are sprung between the rigid outer dome of the faceted cornea and the inner retinal floor in a cage of specialized cell-cell junctions (Cagan and Ready, 1989) (Fig. 1). Tension in the convex retinal floor stretches the rhabdomere cage on the longitudinal axis, which aligns rhabdomeres, and must be balanced with growth and renewal of rhabdomeres across the retina (Raghu et al., 2009).

The reduction in the basal surface is largely powered by actin stress fibers and the associated non-muscle myosin II in IOC endfeet, as eyes deficient in *zipper* (*zip*; myosin II heavy chain) and actin regulation contain distorted retinal floors (Baumann, 2004; Cagan and Ready, 1989; Galy et al., 2011; Longley and Ready, 1995). At the mid-pupal stage, stress fibers form at the IOC endfeet and are anchored to the grommets via integrins (Longley and Ready, 1995), appearing as filaments emanating from the grommets. These stress fibers mature through the late pupal stages and generate tension, bringing attached grommets closer together. Concomitant with contraction, stress fibers transform from a looser, filamentous

Department of Biological Sciences, Purdue University, 915 West State Street, West Lafayette, IN 47907-2054, USA.

*Author for correspondence (hcchang@purdue.edu)

 H.C.C., 0000-0002-4939-0463

Handling Editor: Thomas Lecuit

Received 12 April 2021; Accepted 18 October 2021

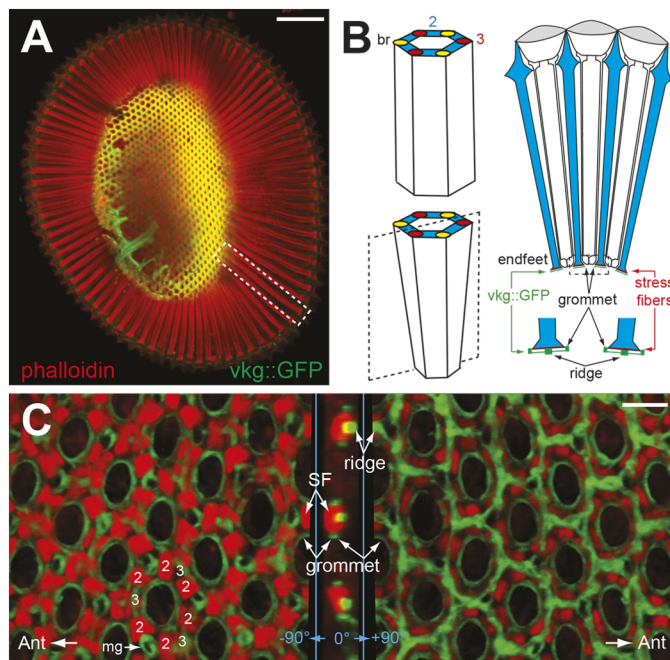


Fig. 1. *Drosophila* eye curvature requires retinal floor condensation.

(A) A 3D rendering from confocal images of a *cn, bw, vkg::GFP* adult retina stained with phalloidin (red). This bottom view reveals the rhabdomeres extended throughout the depth of this convex epithelium (dashed box) and the actomyosin and ECM meshwork at the retinal floor (red and green, center). Because of the retinal curvature, a distal part of phalloidin-stained lamina, situated beneath the basement membrane, is included. In addition, a GFP-positive trachea is seen at the posterior edge of the basement. Scale bar: 50 μ m. (B) Left: Schematic showing a hexagonal column, consisting of secondary (2, blue), tertiary (3, red) pigment cells, and bristle cells (br, yellow), with and without basal reduction. Right: A cross-section drawing (angle of the section indicated with a dashed box on the left) showing the secondary pigment cell (blue) endfeet of three adjacent clusters. IOC endfeet, standing upon the planar basement membrane ECM, are organized as grommets and ridges (green). Actin stress fibers (red lines) within the endfeet are anchored to adjacent grommets. Corneal lenslets are indicated by gray ovals. (C) A floor triptych rendered from confocal stacks of *cn, bw, vkg::GFP* adult retina, stained with phalloidin (red). Left: A view from within the retina, showing the stereotypical arrangement of dense stress fiber patches (SF) in the endfeet of secondary and tertiary pigment cells. Bristle axons exit the retina via mini grommets (mg). Middle: The reconstruction edge-on view at the indicated cut (blue lines). Right: A bottom view revealing retinal ECM organized in grommets and ridges. Ridges join to form a hexagonal network. Scale bar: 5 μ m.

organization to larger, dense patches with higher levels of stress fibers abutting the neighboring grommets (partially contracted), and then to small, dense patches connecting the grommets (fully contracted). Thus, the contraction of endfeet stress fibers, manifested by a progressive reduction of their sizes, compacts the fenestrated membrane, including the ECM below. The regular organization of the ommatidia is preserved at the retinal floor, suggesting that the tensile forces for reducing the IOC endfeet are precisely applied.

To decipher the mechanism coordinating IOC endfeet contraction, we have combined live imaging with a Ca^{2+} sensor (Chen et al., 2013) and mutational analysis to investigate Ca^{2+} signaling in non-neuronal retinal cells. Ca^{2+} is a ubiquitous and versatile second messenger, impacting virtually all cell physiologies (Berridge et al., 2000). In addition to facilitating muscle contraction, Ca^{2+} signaling participates in actin remodeling and contraction in non-muscle cells. Ca^{2+} -dependent regulation of non-muscle myosin II, a hexamer of two heavy chains, two regulatory light chains (MRLC), and two essential light chains, has been well characterized

(Brito and Sousa, 2020; Heissler and Sellers, 2016). Myosin II activity is increased by the phosphorylation of MRLC, which can be upregulated by calmodulin-dependent myosin light chain kinase (MLCK) in response to Ca^{2+} signaling (Scholey et al., 1980; Heissler and Sellers, 2016). Thus, orchestrated Ca^{2+} signaling, such as a propagation of Ca^{2+} spikes through constituent cells, is capable of coordinating the activity of actomyosin networks in tissue morphogenesis (Homolya et al., 2000). In *Drosophila* egg activation, a single Ca^{2+} wave leads to actin reorganization and the formation of dynamic actin around the cell cortex (York-Andersen et al., 2015, 2020; Kaneuchi et al., 2015). In wing discs, oscillating Ca^{2+} waves influence actomyosin organization (Balaji et al., 2017) and facilitate recovery in response to mechanical injury (Brodskiy et al., 2019; Narciso et al., 2017; Restrepo and Basler, 2016). In vertebrate epithelia, Ca^{2+} propagation induces actin rearrangement in the surrounding cells to promote cell extrusion (Takeuchi et al., 2020).

In mammalian retina, Ca^{2+} signaling is known to facilitate the formation of electrical synapses and mediates trophism between supporting cells and neurons (Barres, 2008; Allaman et al., 2011; Halassa and Haydon, 2010; Fields and Stevens-Graham, 2002). In addition, intercellular propagations of Ca^{2+} spikes sweep across glial cell networks, including astrocytes in the central nervous system (Cornell-Bell et al., 1990) and Müller retinal glial cells (Kurth-Nelson et al., 2009), although the roles of Ca^{2+} waves in these cells remain unresolved (Scemes and Giaume, 2006). In *Drosophila* retina, Ca^{2+} has crucial functions in phototransduction (Voolstra and Huber, 2020; O'Tousa, 2002) and Ca^{2+} dynamics in isolated live photoreceptors have been recorded (Asteriti et al., 2017; Hardie, 1996). Stimulus-independent Ca^{2+} oscillations have also been observed in developing photoreceptors and are thought to facilitate neuronal connections (Akin et al., 2019; Choi et al., 2021). The versatility of Ca^{2+} signaling and its known impact on actomyosin activity make it a good candidate for orchestrating endfeet stress fiber contraction, although whether Ca^{2+} signaling has a role in accessory cells in fly retina is not known.

Here, we report a novel observation: Ca^{2+} waves regularly sweep across the eye's honeycomb-like lattice of IOCs. These waves, formed during pupal development, require *IP3R* (*Itrp*), indicating that IOC Ca^{2+} waves are mediated by Ca^{2+} release from internal stores. Mutational analysis of *IP3R* suggests that Ca^{2+} waves contribute to the retinal floor reduction by facilitating the contraction of actin stress fibers at the IOC endfeet. Our work suggests a mechanism by which intercellular Ca^{2+} waves coordinate contractile forces for an orderly retinal floor condensation. Moreover, absence of *IP3R* results in a deformed fenestrated membrane ECM, indicating that contractile forces from the endfeet stress fibers shape the ECM network.

RESULTS

A model for visualizing intracellular Ca^{2+} levels in *Drosophila* retina

To monitor the intracellular Ca^{2+} levels in developing and adult *Drosophila* eyes, we expressed GCaMP6m (Chen et al., 2013) with *longGMR-GAL4* (Wernet et al., 2003), hereafter referred to as *IGMR>GCaMP6m*. Like the more widely used *GMR-GAL4* (Freeman, 1996), *IGMR-GAL4* becomes active in cells posterior to the MF and remains active in most of the retinal cells at subsequent stages (except the bristle cells). We chose *IGMR-GAL4* because its moderate GAL4 expression level, compared with *GMR-GAL4*, is less likely to cause cytotoxicity (Bollepalli et al., 2017; Kramer and Staveley, 2003), which may damage the eye architecture and

indirectly perturb the cellular Ca^{2+} level. To minimize potential toxicity and artifact from high GAL4 expression, all *IGMR>GCaMP6m* recordings presented in subsequent sections were performed with heterozygotes.

Using this *IGMR>GCaMP6m* platform, we analyzed the spatiotemporal pattern of cytosolic Ca^{2+} increases in non-neuronal supporting cells, namely IOC cells, primary pigment cells and cone cells. As the composition, arrangement and architecture of these accessory cells are well established (Cagan and Ready, 1989), we imaged *IGMR>GCaMP6m* retinas at different focal planes to monitor their respective Ca^{2+} activities.

Ca^{2+} waves propagate through interommatidial cells

Imaging young *IGMR>GCaMP6m* adult retina at the distal plane showed that Ca^{2+} waves propagate regularly across the hexagonal IOC lattice (hereafter referred to as IOC waves; Fig. 2A, Movie 1). We tracked the movement of the wave fronts by sequentially subtracting signal intensities from consecutive images of the time-lapse series. This revealed that the initiation of IOC waves was not restricted to a specific region. For instance, the IOC waves in Movie 1 could initiate from the middle ($t=80$ s), anterior ($t=4$ s, 152 s, 210 s, 266 s), anterior-dorsal ($t=92$ s), posterior-ventral ($t=14$ s) and posterior-dorsal ($t=20$ s) edges of this *IGMR>GCaMP6m* retina (Fig. 2B). Once initiated, the IOC waves moved equally in all directions across the eye field (Fig. 2C). Each IOC spiked approximately 2 s after a neighboring cell, translating to a wave speed of 4–5 $\mu\text{m}/\text{s}$. When two IOC waves collided, the wave fronts merged and advanced toward regions where the cells had yet to experience recent Ca^{2+} waves (Fig. 2D). If no such region was available, the colliding IOC waves ceased (Fig. 2D). The GCaMP6m intensity at the juncture of merging wave fronts was not greater than those before the collision, implying that one or more factors responsible for triggering IOC Ca^{2+} waves are limiting, rendering these cells unresponsive to an additional dose of wave-inducing signal.

The characteristics of Ca^{2+} spikes within these IOC waves were remarkably consistent (Fig. 2E). In Movie 1, all 273 cells (204 secondary and 69 tertiary pigment cells) exhibited regular calcium oscillations (average peak number was 4.8 ± 0.4 , $n=273$) during the 5-min recording. These reproducible Ca^{2+} spikes rose sharply to a maximum in approximately 6.8 ± 2.2 s (T_{on} , i.e. time from baseline to peak; $n=1309$ peaks) with a slower return to baseline (25.1 ± 3.8 s; T_{off} , i.e. time from peak to baseline). The interval time, measured as the duration from one peak to the subsequent peak, was 68.6 ± 12.4 s. The peak intensities of Ca^{2+} spikes experienced by individual cells showed no apparent dampening over time. No noticeable difference in Ca^{2+} spike characteristics was seen between secondary and tertiary pigment cells (Fig. S1B) or between cells from different regions (Fig. S1C). Pair-wise Pearson correlation analysis performed on the numeric series generated from GCaMP6m intensity over time indicated that the cells were most related to their adjacent cells, further confirming the wave-like nature of these Ca^{2+} spikes (Fig. S1D). To demonstrate that these descriptions are representative, we present the analysis of IOC waves (one still image shown in Fig. 5D) from an independently acquired *IGMR>GCaMP6m* recording in Fig. S2 ($n=474$ cells).

IOC waves include primary pigment cells, but not cone cells

To determine whether other accessory cells contribute to IOC waves, we imaged young *IGMR>GCaMP6m* retinas more proximally, where Ca^{2+} increases in IOC waves, although not easily attributable to individual cells, were still recognizable (Fig. 3A). In

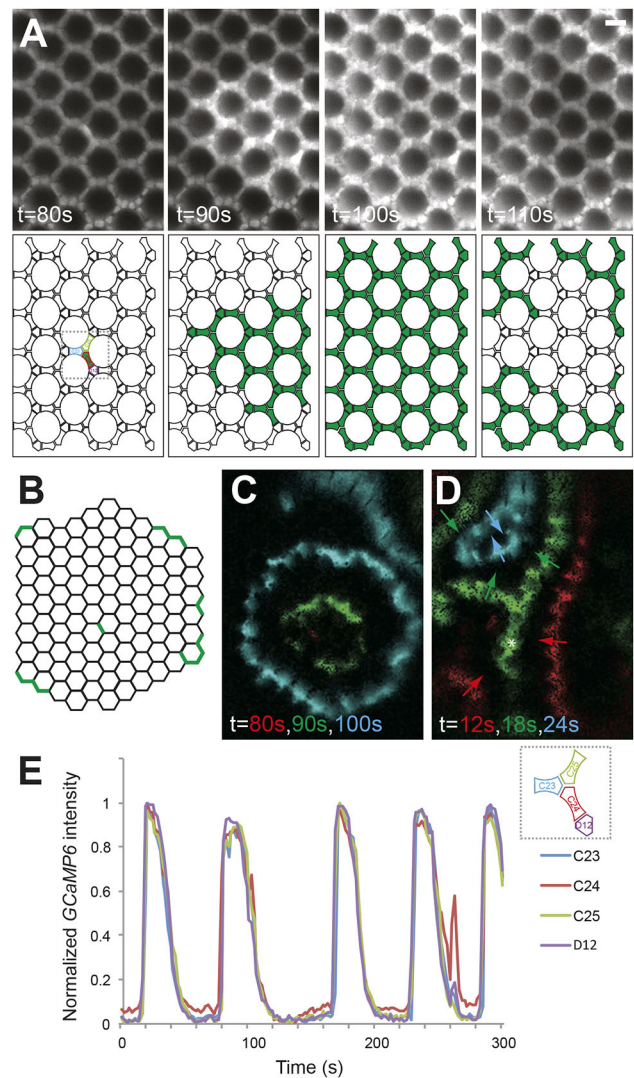


Fig. 2. Ca^{2+} waves propagate regularly through IOC cells. (A) Top row: A montage showing a Ca^{2+} wave initiated at $t=80$ s in a 1-day-old *IGMR>GCaMP6m* retina. Bottom row: Schematics of the micrographs above, showing the IOCs experiencing Ca^{2+} waves (green). Bristle cells are omitted from the drawings. Scale bar: 10 μm . (B) Schematic of the IOC wave origins, each denoted with a green line. For those IOC waves moving from the edges, the exact origin cells cannot be determined and the first cells with Ca^{2+} increases when these waves come into view are indicated. (C) An image overlaying three wave fronts (generated by intensity subtraction of consecutive images) at $t=80$ s (red), 90 s (green) and 100 s (blue), respectively. This IOC wave (the same one as shown in A), initiated at $t=80$ s, propagates in all directions at 5 $\mu\text{m}/\text{s}$. At $t=100$ s, a distinct wave front approaches from the anterior-dorsal edge. (D) An image overlaying three wave fronts at $t=12$ s (red), 18 s (green) and 24 s (blue), respectively (wave directions are indicated by arrows). At $t=12$ s, two wave fronts approach from anterior and posterior-ventral edges. At $t=18$ s, these two wave fronts merge into one (the merging site is indicated by an asterisk) and move dorsally, and a distinct wave approaches from the posterior-dorsal edge. At $t=24$ s, all these waves merged to form a centripetal front. (E) Plot of normalized GCaMP6m intensity $[(F - F_{\text{min}})/(F_{\text{max}} - F_{\text{min}})]$ over time showing the regular Ca^{2+} oscillation in four cells, color-labeled and bracketed by a gray dashed box in the left-most schematic in A (C23, C24 and C25 are secondary pigment cells, whereas D12 is a tertiary pigment cell).

this plane, *GCaMP6m* signals in the nuclei of primary pigment cells, the two crescent-shaped cells situated apically between the IOCs and cone cells, were particularly noticeable, possibly owing to

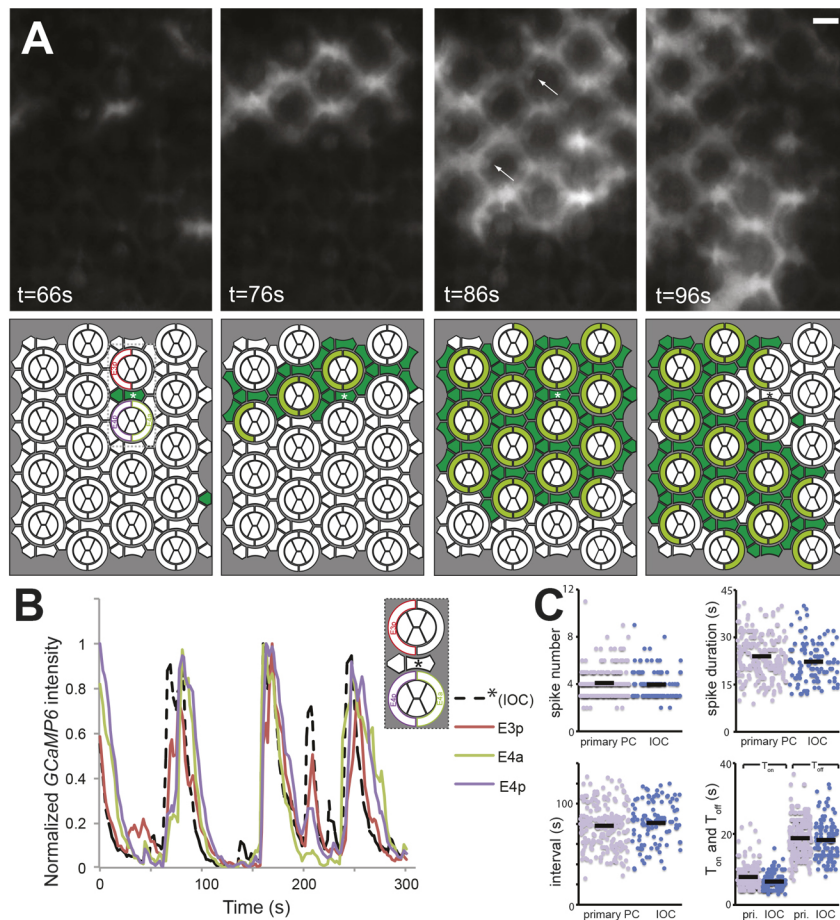


Fig. 3. Primary pigment cells, but not cone cells, are a part of the IOC wave network. (A) Top row: A young *IGMR>GCaMP6m* retina imaged at a proximal plane, showing an IOC wave initiated from a secondary pigment cell (asterisk in the schematic below) at $t=66$ s traversing through the primary pigment cells. In primary pigment cells, the GCaMP6m signals in the nuclei are stronger than those seen in the cytoplasm (arrows). Bottom row: Schematics showing the four pie-slice-shaped cone cells, the two crescent-shaped primary pigment cells, and the interommatidial secondary and tertiary pigment cells. IOC and primary pigment cells experiencing Ca^{2+} waves are highlighted in dark green and light green, respectively. As GCaMP6m signals from secondary and tertiary pigment cells at this plane are hazy, those assigned to exhibit Ca^{2+} increases are approximations. Scale bar: 10 μm . (B) Plot of normalized GCaMP6m intensity over time showing the Ca^{2+} oscillation in one secondary (dashed black line; from the cell marked with black asterisk in A) and three primary (solid color lines; from cells labeled with corresponding color and bracketed by a gray dashed box in A; E4a is an anterior primary pigment cell, whereas E3p and E4p are posterior primary pigment cells) pigment cells. (C) Scatter plots of Ca^{2+} spike characteristics from primary pigment cells ($n=214$ cells, purple dots) and IOCs ($n=109$ cells, blue dots) of this recording. Dots represent the spike numbers, spike duration averages, interval averages, and T_{on} and T_{off} averages in individual cells. Averages from all IOCs or primary pigment cells are indicated by black bars. PC, pigment cell.

quenching of the *GCaMP6m* fluorescence in the cytoplasm by the pigment granules (Fig. 3A). From two independent recordings (Movies 2 and 3), *GCaMP6m* signals in the primary pigment cells increased synchronously with IOC wave passages (Fig. 3A,B, arrows; Fig. S3A,B), demonstrating that the IOC wave network includes the primary pigment cells. In support of this, the characteristics of Ca^{2+} spikes in primary pigment cells resembled those observed in the secondary and tertiary pigment cells (Fig. 3C, Fig. S3C).

In contrast, cone cells, the four cells situated centrally atop the photoreceptors, exhibited Ca^{2+} activities that were independent of the IOC waves (Fig. 4A, Movie 4). Cone cell Ca^{2+} spikes were readily seen without an adjacent IOC wave, and, conversely, many cone cells were silent when IOC waves passed by (two such examples are indicated by arrows at 28 s). Whereas all secondary and tertiary pigment cells participated in propagating the IOC waves, not all cone cells were active during the 5-min recording (Fig. 4B). Of the 141 clusters analyzed, in only 51 (35.7%) did all four cells exhibit Ca^{2+} transients (Fig. 4C), and tabulation of the distribution indicated that 124 of the 564 (22.0%) cone cells were inactive. Moreover, the cone cell Ca^{2+} spike characteristics were noticeably different from those of IOC waves (Fig. 4D). For instance, from this recording, Ca^{2+} spikes ($n=280$) from 39 randomly selected IOC cells had a T_{on} of 12.03 ± 8.37 s and a T_{off} of 22.18 ± 8.45 s. In contrast, cone cell Ca^{2+} spikes ($n=6179$) had a shorter duration, with a T_{on} of 2.36 ± 0.34 s and a T_{off} of 3.50 ± 1.04 s. These Ca^{2+} spike differences, along with the lack of apparent coordination, demonstrate that IOC waves and cone cell Ca^{2+} spikes are separate events.

Interestingly, cone cells within a given cluster showed coordinated Ca^{2+} spikes. One example is shown in Fig. 4E, in which a cone cell Ca^{2+} spike initiated at $t=86$ s (arrow) and swept through the adjacent two cells in successive time frames. This suggests that cone cells in each cluster form their own mini wave network, independently of the IOC waves and other clusters. In support of this, pair-wise Pearson analysis of GCaMP6m signal over time with cone cells of the same cluster showed higher correlations than with those from different clusters (Fig. 4F).

IOC waves start at the late pupal stage and persist in older flies

To understand how these Ca^{2+} wave networks are constructed, we characterized the onset and pattern of GCaMP6m signals in developing retinas. Ca^{2+} waves were observed in *ey>GCaMP6m* eye discs behind and ahead of the MF (Fig. S4; Movie 5). The eye disc is highly dynamic with multiple developmental events compressed in a strong temporal gradient (Roignant and Treisman, 2009; Tsachaki and Sprecher, 2012; Wolff and Ready, 1991). Accordingly, we focused on Ca^{2+} activities in the latter half of pupal development, when pattern formation is complete (Cagan and Ready, 1989) and the temporal gradient has flattened, i.e. all cells are developing on the same timeline. At the P9 to P10 stages, *IGMR>GCaMP6m* retina showed no detectable Ca^{2+} activity (not shown). At the P12 stage, although most of the cells were still silent, Ca^{2+} activities in isolated IOCs and cone cells began to emerge (Fig. 5A, Movie 6). Furthermore, instances of Ca^{2+} waves propagating between adjacent IOC cells were seen (Fig. 5A,B), suggesting that the formation of IOC wave network had

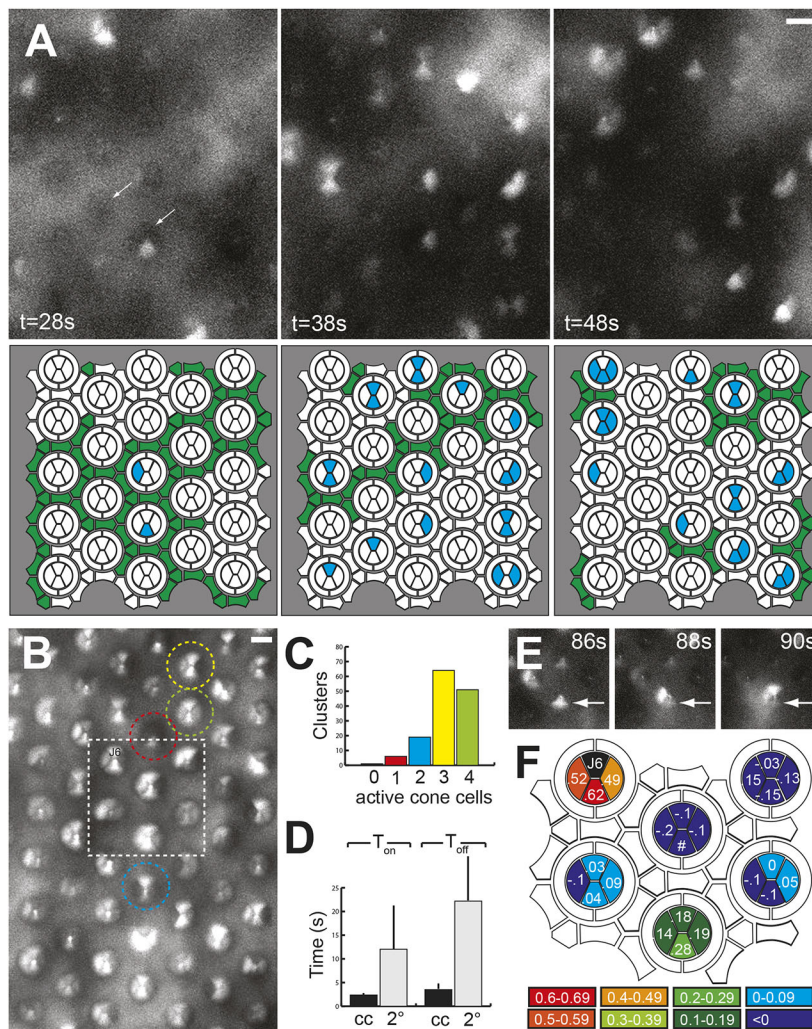


Fig. 4. Cone cells exhibit Ca²⁺ activities distinct from the IOC waves. (A) Top row: A young *IGMR>GCaMP6m* retina showing Ca²⁺ activities in cone cells. Arrows indicate inactive cone cells when an IOC wave passes by. Bottom row: IOC and cone cells experiencing Ca²⁺ waves are highlighted in green and blue, respectively. The secondary and tertiary pigment cells assigned to display Ca²⁺ spikes are approximations. Scale bar: 10 μ m. (B) Maximum intensity projection of the same *IGMR>GCaMP6m* retina as shown in A. Examples of clusters with one (red), two (blue), three (yellow) and four (green) *GCaMP6m*-active cone cells are labeled with dashed circles. Scale bar: 10 μ m. (C) Quantification of the clusters shown in B, with the same color code. (D) The Ca²⁺ spikes in cone cells ($n=564$ cells measured from Movie 4) have shorter T_{on} and T_{off} averages than the surrounding IOCs ($n=39$ IOCs selected for measurement from the same recording). (E) A cropped montage showing a Ca²⁺ spike, initiated at t=86 s in an equatorial cone cell (arrow), sweeping through two cone cells of the same cluster. (F) Schematic map showing pair-wise Pearson correlation analysis performed on numeric series generated from *GCaMP6m* intensities over time with cell J6 (black; labeled in B). The region containing the analyzed clusters corresponds to the dashed box in B.

commenced. Imaging the same eye 1 day later showed widespread IOC waves and cone cell blinking (Fig. 5C, Movie 7), suggesting that the construction of the entire IOC wave network took place within this time.

To determine whether these Ca²⁺ events deteriorate with age, we analyzed *IGMR>GCaMP6m* retinas from older flies. Young retina, as mentioned above, showed regular IOC waves and cone cell blinking (Fig. 5D). Whereas cone cell Ca²⁺ spikes ceased about 5 days after eclosion, IOC waves were still present in 10- and 21-day-old *IGMR>GCaMP6m* retinas (Fig. 5E,F). However, compared with the waves in younger retina, IOC waves in older flies appeared to be irregular, evidenced by the decrease in peak number and the large variation in spike intervals (Fig. 5G).

IOC waves are independent of phototransduction

Because the pigment and cone cells surround the photoreceptors, we asked whether the above-mentioned Ca²⁺ events require phototransduction. Prior to each recording session, dark-adapted *IGMR>GCaMP6m* retina was illuminated with 647 nm light pulses to inactivate the metarhodopsin in photoreceptors. Nonetheless, IOC waves were often present immediately at the start of recording, suggesting that waves were spontaneous and ongoing in the dark. Still, we frequently observed a surge in the overall eye brightness with multiple waves merging to cover the whole retina within the

first 30 s following illumination, suggestive of initial *GCaMP6m* signal being influenced by light. To test definitively whether the occurrence of IOC waves requires phototransduction, we monitored *IGMR>GCaMP6m* signals in retina mutant for *norpA*, the *Drosophila* phospholipase C β homolog known for its role in acting downstream of the rhodopsin (Bloomquist et al., 1988). We reasoned that if the initiation or propagation of IOC waves requires phototransduction, *GCaMP6m* signals should be absent or noticeably reduced in *norpA*. Although eyes mutant for *norpA*³⁶, a complete loss-of-function allele, displayed no response to light stimulation (Pearn et al., 1996), robust IOC waves were seen in *norpA*³⁶ (Fig. 6A, Movie 8) and the Ca²⁺ transient profiles were similar to those observed in wild type (Fig. 6B). These results demonstrate that IOC waves are independent of phototransduction.

IOC waves and cone cell Ca²⁺ activities both require *IP3R*

Based on the fast speed (4–5 μ m/s) of IOC waves (Jaffe, 2008), we speculated that the source for the IOC Ca²⁺ waves is IP3R-regulated Ca²⁺ release from the endoplasmic reticulum (ER) stores. To test this, we monitored *GCaMP6m* signals in retinal cells mutant for *l(3)itpr*^{90B.0}, a complete loss-of-function allele of *IP3R* (Venkatesh and Hasan, 1997). As *IP3R* is an essential gene, mosaic eyes containing clones of homozygous *l(3)itpr*^{90B.0} cells, marked by the absence of a membrane-associated mRFP (Chang et al., 2002), were

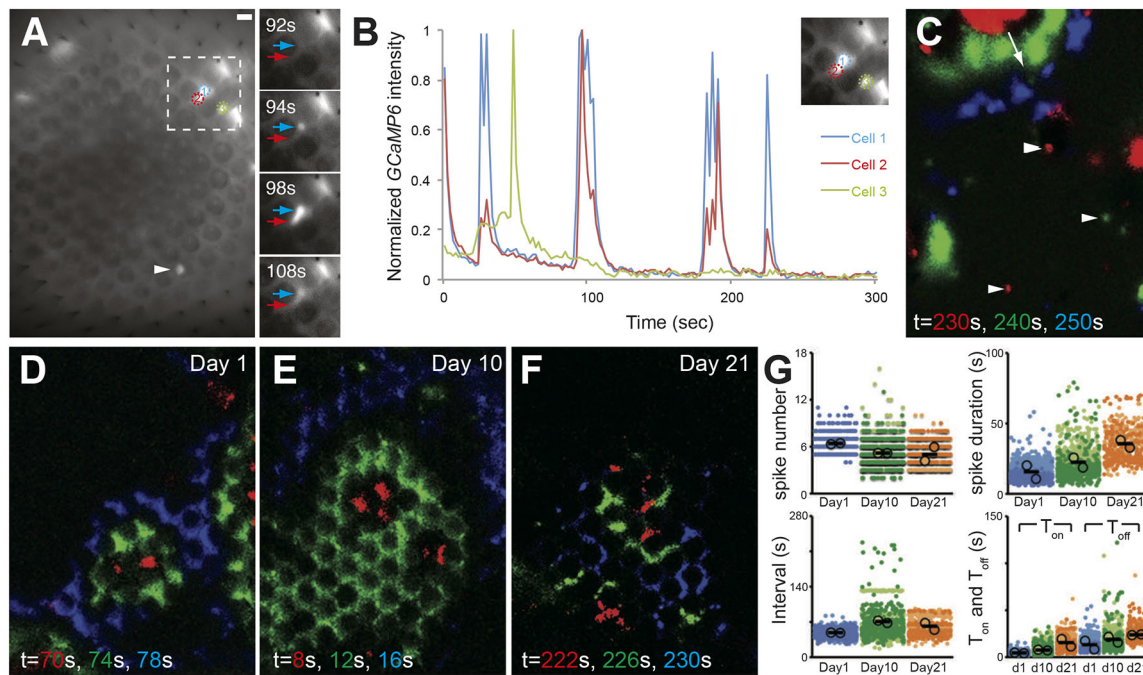


Fig. 5. IOC waves emerge at the late pupal stage. (A) Maximum intensity projection from a *IGMR>GCaMP6m* pupal eye at P12 stage. Although most of the cells were inactive, a few IOCs [two tertiary pigment cells indicated with blue (Cell 1) and green (Cell 3) circles and one secondary pigment cell (Cell 2) indicated with a red circle] and cone cells (arrowhead) exhibited Ca^{2+} transients. A region (dashed box) containing a two-cell 'wave' is shown at a higher magnification. At $t=94$ s, a tertiary pigment cell (Cell 1, blue arrow) experienced a Ca^{2+} increase, which was followed by a spike in an adjacent secondary pigment cell (Cell 2, red arrow) at $t=98$ s. Scale bar: 10 μm . (B) Plot of normalized GCaMP6m intensity over time showing the Ca^{2+} oscillations in these two cells (blue and red), but not Cell 3 (green), were coordinated. (C) An image overlaying three wave fronts from the same retina as shown in A imaged 1 day later. An IOC wave (arrow), initiated at the dorsal edge at $t=230$ s (red), was seen propagating ventrally. In addition, Ca^{2+} spikes in cone cells were readily seen (arrowheads). (D-F) Overlaid images showing wave fronts at 4 s intervals from 1-day-old (D), 10-day-old (E) and 21-day-old (F) *IGMR>GCaMP6m* retina. (G) Superplots (Lord et al., 2020) comparing spike characteristics of aging *IGMR>GCaMP6m* retinas at 1 day [light blue ($n=424$ cells) and blue ($n=388$ cells) dots represent numbers from individual IOCs of two independent eyes], 10 days [light green ($n=464$) and green ($n=388$) dots] and 21 days [beige ($n=246$) and orange ($n=215$) dots]. Averages from IOCs of the same retina are indicated by solid circles of corresponding colors, and averages from different age groups are indicated by black bars.

generated by FLP-induced recombination (Fig. 6C, Movie 9). Robust IOC waves were seen in wild-type cells (*mRFP⁺*), but did not traverse into *l(3)itpr^{90B.0}* mutant territory (Fig. 6D), indicating that IP3R function is required for wave propagation. Moreover, no GCaMP6m flash was observed in *l(3)itpr^{90B.0}* cells, suggesting that IOC wave initiation, like propagation, requires IP3R function.

This mosaic eye contained two wild-type patches partitioned by an *IP3R⁻* clone, allowing us to investigate the behavior of IOC waves from two separate populations in the same retina. As shown in Fig. 6E, IOC waves in the larger clone had more Ca^{2+} spikes (4.0 ± 1.2 , $n=210$) than the waves in the small clone near the dorsal posterior region (2.4 ± 0.9 , $n=21$). In addition, the Ca^{2+} spikes from these two clones occurred at different time points, indicating that the IOC waves could arise independently in separate cell populations.

At this focal plane, although the identity of specific cone cells experiencing Ca^{2+} spikes cannot be ascertained (because they were out of focus), wild-type clusters with cone cell Ca^{2+} activities were still discernible (Fig. 6D, arrowheads). In comparison, such clusters were completely absent in *IP3R⁻* cone cells (Fig. 6F), demonstrating that both IOC waves and cone cell Ca^{2+} activities require internal Ca^{2+} release.

IP3R mutation disrupts IOC endfeet stress fiber morphology and retinal floor condensation

To understand the functional relevance of IOC waves, we looked for morphological defects associated with *IP3R⁻* IOCs. As removal of *IP3R* function has no effect on the retinal cell fate (Acharya et al.,

1997; Raghu et al., 2000), we suspected that the *IP3R⁻* mutation perturbs specific subcellular structures in IOCs. To investigate whether the *IP3R⁻* mutation affects the actin stress fibers at the endfeet, adult *l(3)itpr^{90B.0}* mosaic eyes were stained with phalloidin to label the filamentous actin. These eyes were also rendered pigmentless with *cn* and *bw* mutations to eliminate interference from the pigment granules during imaging. In wild-type clones, dense patches of fully contracted stress fibers surrounded and interconnected the grommets (Fig. 7A-C, arrows). In contrast, stress fibers in *l(3)itpr^{90B.0}* mutant cells, marked by the absence of *ubi-mRFP^{nl}*, exhibited various degrees of abnormalities. In some *IP3R⁻* cells, especially those in smaller clones (asterisk marks an example in Fig. 7E), the stress fibers retained the patched morphology although their sizes were enlarged. In others, the defect was more severe, as the stress fibers, although still anchored to the grommets, appeared frayed, stretched and unbundled (Fig. 7C, arrowheads).

To determine whether this disruption of endfeet stress fibers affects the retinal floor area, we measured the cluster area, defined by a hexagon generated by connecting the centers of the six adjacent clusters (Fig. 7D,E). Mosaic eyes containing only wild-type clones showed no difference in the size of these hexagons, demonstrating that FLP-induced mitotic recombination had no influence on the retinal floor area (Fig. 7F). In contrast, in mosaic eyes containing *IP3R⁻* clones, the retinal floor area per cluster in mutant patches was $\sim 40\%$ larger than their sibling wild-type clones. This perturbation of area size in *IP3R⁻* clones is specific to the retinal floor, as the apical area (the cornea level) in *IP3R⁻* clones remained unaffected.

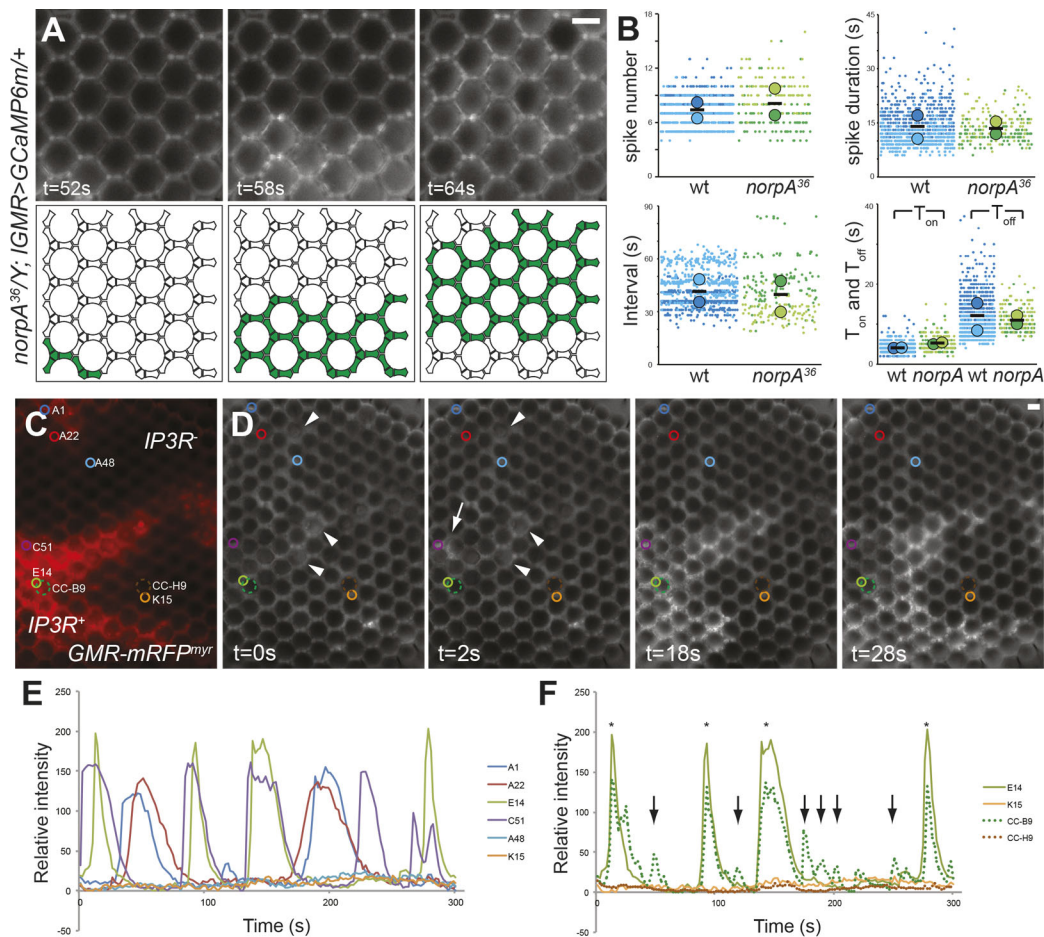


Fig. 6. IOC waves are independent of phototransduction but require IP3R. (A) Top row: A montage showing an IOC wave moving across a young *norpA*³⁶ retina. Bottom row: Schematics showing the IOCs experiencing Ca²⁺ waves (green). Scale bar: 10 μ m. (B) Superplots of IOC spike characteristics from wild-type [blue ($n=444$) and light blue ($n=388$) dots represent numbers from individual IOCs of two independent eyes] and *norpA*³⁶ [green ($n=124$) and light green ($n=96$) dots] retinas. Averages from IOCs of the same retina are indicated by solid circles of corresponding colors, and averages from all IOCs of the same genotype are indicated by black bars. Paired, two-tailed *t*-tests [two retinas of each genotype ($n=2$); *P*-values: 0.76 for spike number, 0.98 for spike duration, 0.86 for interval, 0.10 for T_{on} and 0.90 for T_{off}] suggest that wild-type (wt) and *norpA*³⁶ IOC waves are not significantly different. (C) A mosaic [*ey-FLP*+/+; *IGMR>GCaMP6m*/+; *FRT*^{82B}; *l(3)itpr*^{90B.0}/*FRT*^{82B}; *GMR-mRFP*^{myr}] eye containing *IP3R*⁺ and *IP3R*⁻ patches, labeled by the presence and the absence of membrane-associated mRFP (myristylated mRFP), respectively. Cells selected for GCaMP6m intensity analysis are labeled and marked by colored circles. (D) A montage of GCaMP6m signals from the same eye. The IOCs were inactive at $t=0$ s, and a Ca²⁺ wave initiated at the posterior edge at $t=2$ s (arrow) propagated only in the IOCs within the large *IP3R*⁺ clone. Ca²⁺ activities in cone cell clusters (arrowheads) could also be discerned. Scale bar: 10 μ m. (E) Plot of GCaMP6m intensity ($F-F_{min}$) over time in six IOCs (labeled by solid color circles in A) showing robust Ca²⁺ oscillation in the four *IP3R*⁺ cells, but baseline in the two *IP3R*⁻ cells. It is notable that the IOCs from distinct *IP3R*⁺ clones (the red and blue cells from the smaller clone near the posterior-dorsal border, and the green and purple cells from the central large clone) exhibited different patterns of Ca²⁺ spikes. (F) Plot of GCaMP6m intensity over time in two cone cell clusters (labeled by dashed color circles in A; we quantified signal intensities from these cell clusters because the cone cells were out of focus and could not be individually identified). As IOC wave passage masks the GCaMP6m signals in cone cell clusters (asterisks), we compared the detection of Ca²⁺ spikes in *IP3R*⁺ and *IP3R*⁻ clusters during the absence of IOC wave (arrows). Intensity plots of two IOCs (green and orange solid circles; both are shown in C) adjacent to selected cone cell clusters are shown as reference.

IP3R mutation affects endfeet stress fiber contraction

The aberrant stress fibers in adult *IP3R*⁻ cells could be caused by a block in the progression of stress fiber contraction during pupal development or an inability to maintain the contracted fibers in adults. To distinguish between these possibilities, we monitored stress fiber morphology in pupal *IP3R*⁻ mosaic eyes. If the role of IP3R is limited to maintaining contracted stress fibers in adults, stress fibers in *IP3R*⁻ mutant pupal eyes should appear normal. In a *l(3)itpr*^{90B.0} mosaic eye at ~75% pupal development, the endfeet stress fibers in wild-type cells were partially contracted, appearing as two discrete patches next to adjacent grommets (Fig. 7G-I, double arrows). In comparison, stress fibers in *IP3R*⁻ mutant cells were frayed and unbundled (Fig. 7G-I, arrowheads), indicating that IP3R is required for the progression of endfeet stress fiber contraction. It is

noteworthy that the stage at which this phenotype is observed coincides well with the onset of IOC waves.

IP3R loss perturbs basement membrane collagen IV

To investigate the effect of stress fiber deficits on the underlying ECM, we used *Vkg::GFP* (Kelso et al., 2004), which fluorescently tags endogenous *Drosophila collagen IV $\alpha 2$* (*viking*) (Yasothornsrikul et al., 1997), a ubiquitous, network-forming basement membrane component (Kefalides, 1973; Brown et al., 2017; Fidler et al., 2017). In wild-type adult retina, basement membrane *Vkg::GFP* is organized in grommets and ridges (Fig. 1B,C). Compared with wild type, *Vkg::GFP* signal intensity in *IP3R*⁻ clones was reduced (Fig. 8A-D). Mean intensity measurement of *Vkg::GFP* showed a 32% reduction in the

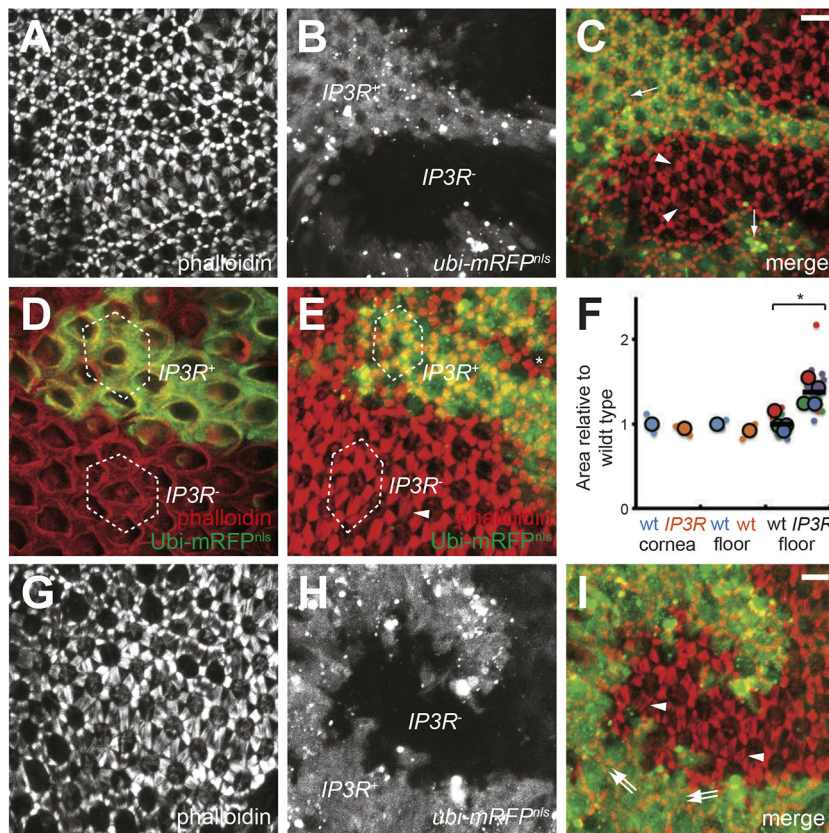


Fig. 7. IOC endfeet stress fiber contraction and retinal floor condensation are disrupted in *IP3R* clones. (A-C) Maximum intensity projections of confocal sections (along the z-axis) of *ey-FLP; cn, bw; FRT^{82B}, l(3)itpr^{90B.0}/FRT^{82B}, ubi-mRFP^{nlis}* adult eye stained with phalloidin (A; red in C). This *IP3R*⁻ mosaic eye contains *IP3R*⁺ and *IP3R*⁻ patches, labeled by the presence and the absence of mRFP (B; green in C), respectively. Arrows and arrowheads in C indicate wild-type stress fibers and frayed, stretched, and unbundled stress fibers in mutant clones, respectively. Scale bar: 10 μ m. (D-F) To measure the effect of *IP3R*⁻ on the retinal floor area, hexagonal regions (D,E; dashed lines), generated by connecting the centers of six adjacent clusters were quantified (F). Individual hexagonal area measurements from four mosaic eyes, normalized to the wild-type average, are represented by color-coded dots (red, green, purple and blue). Area averages from different retinas are indicated by circles of corresponding colors, and averages of different genotypes (a total of 14 wild-type and 18 *IP3R*⁻ hexagonal regions) are indicated by black bars. **P*=0.0082 (Student's *t*-test; *n*=4 retinas). Hexagonal regions at the cornea level [D; three wild-type (blue) and six *IP3R*⁻ (orange) regions from one mosaic retina] and in wild-type clones at the floor level [two wild-type (blue) and four wild-type (orange) regions from one mosaic retina] are included as controls. (G-I) Maximum intensity projections of confocal sections of a mosaic retina at ~75% pupal development stained with phalloidin (G; red in I). The *IP3R*⁺ and *IP3R*⁻ patches are labeled by the presence and the absence of mRFP (H; green in I), respectively. At this stage, the actin stress fibers within each *IP3R*⁺ IOC have not yet consolidated into one single structure, thus appearing as two distinct patches abutting adjacent grommets (double arrows). In comparison, the stress fibers in *IP3R*⁻ are frayed, appearing as filaments emanating from the grommets (arrowheads). Scale bar: 10 μ m.

abovementioned hexagons in *IP3R*⁻ clones (wild type *n*=2; *IP3R*⁻ *n*=2; number of hexagons). These phenotypes were particularly noticeable in a mosaic cluster (Fig. 8, boxed area), in which the Vkg::GFP intensity was lower on the *IP3R*⁻ side with abnormal floor area and stress fibers. Western blot analysis of whole-head lysates suggested that this reduction in Vkg::GFP intensity was not caused by a decrease in Vkg::GFP expression (Fig. S5). This selective area expansion on the *IP3R*⁻ side also resulted in an apparent shift of grommet position towards the *IP3R*⁺ side. Lastly, the grommet area in *IP3R*⁻ clones was reduced by 27% (Fig. 8E), suggesting that the stress fiber contraction provides a stretch to enlarge the grommet size. Taken together, these observations demonstrate that tensile forces from the stress fibers shape the basement membrane in connection with endfeet contraction (Fig. 8F).

Phosphorylated MRLC level is reduced at *IP3R* mutant retinal floor

To understand how IOC waves regulate the endfeet stress fiber contraction, we stained *l(3)itpr^{90B.0}* mosaic eyes with a rabbit polyclonal antibody against phosphorylated MRLC (p-MLC, Ser-19). Ser-19 phosphorylation in MRLC, a target of MLCK in response to Ca²⁺ signaling, can augment the activity of non-muscle myosin II (Scholey et al., 1980; Heissler and Sellers, 2016). The p-MLC antibody detected signals in both wild-type and *IP3R*⁻ cells at the retinal floor, although p-MLC signal intensity was reduced by 37% in *IP3R*⁻ cells (Fig. 9). This result suggests that IOC waves can impact stress fiber contraction by increasing the level of MRLC phosphorylation.

DISCUSSION

Using *IGMR>GCaMP6m*, we have discovered the presence of intercellular Ca²⁺ waves that spontaneously and regularly sweep across the honeycomb lattice of IOC cells and the primary pigment cells. We provide evidence that this IOC-specific communication is insulated from the cone cell Ca²⁺ spikes and phototransduction but requires *IP3R* function. The IOC waves are formed during pupal development and persist with age. As intercellular propagation of Ca²⁺ increases have been described in glia-glia networks in mammalian retina (Kurth-Nelson et al., 2009), our demonstration shows that communication with Ca²⁺ signaling is likely a fundamental and evolutionarily conserved feature of retinal accessory cells.

In adult *Drosophila* eye, photoreceptors depolarize with Ca²⁺ influx in response to light stimulation (Asteriti et al., 2017). As IOC and cone cells contact the photoreceptors, it seems plausible that the occurrence of IOC waves and cone cell spikes depends, at least in part, on phototransduction. The wave surges observed near the beginnings of recordings further lend support to the notion that IOC waves are influenced by illumination. However, the occurrence of IOC waves was clearly unaffected in a *norpa* null mutant. The characteristics of Ca²⁺ spikes in *norpa*³⁶ retina were comparable to those in wild type, suggesting that the complete removal of a phospholipase C that is essential for phototransduction has no modulatory effect on IOC waves. Moreover, although stimulus-independent Ca²⁺ oscillations in developing photoreceptors have recently been reported (Akin et al., 2019), these Ca²⁺ oscillations occur too early (~55-95 h after pupa formation) to influence the IOC waves, and their Ca²⁺ characteristics show no resemblance to those of

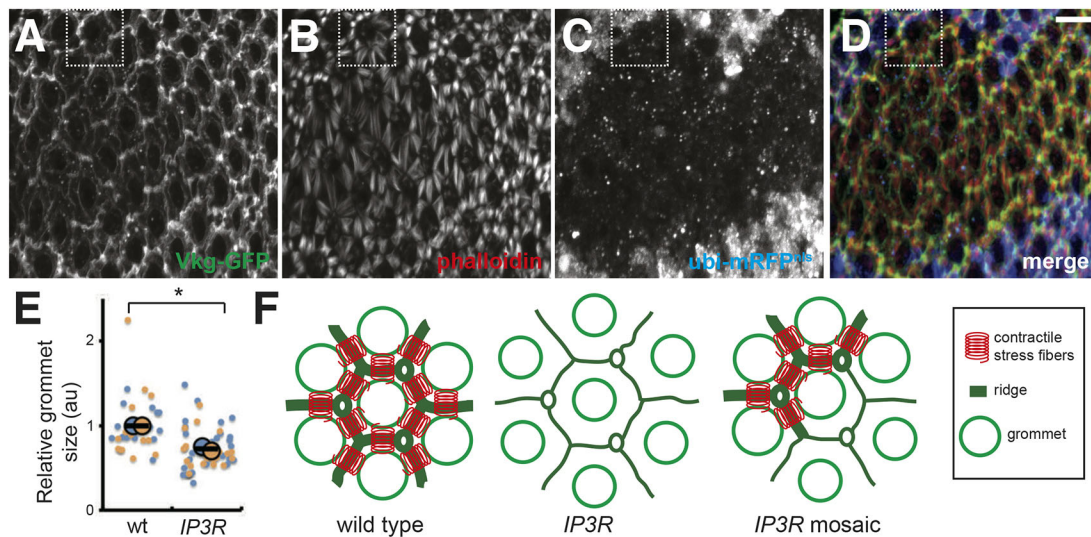


Fig. 8. Vkg::GFP morphology is altered in the *IP3R* mutant. (A–D) Maximum intensity projections of confocal sections of an *ey-FLP; cn, bw, vkg::GFP; FRT^{82B}, I(3)itp^{90B.0}/FRT^{82B}, ubi-mRFP^{nlis}* eye stained with phalloidin (B; red in D). This mosaic eye expresses Vkg::GFP (A, green in D) and contains *IP3R*⁺ and *IP3R*[−] patches, labeled by the presence and the absence of mRFP (C; blue in D), respectively. A cluster containing a mixture of *IP3R*⁺ and *IP3R*[−] cells is highlighted with a dashed box. Scale bar: 10 μ m. (E) Quantification of grommet size in *IP3R*⁺ and *IP3R*[−] patches. Area measurements of individual grommets, normalized to the wild-type average and represented by color-coded dots (beige for eye 1 and blue for eye 2), were obtained from two mosaic eyes (16 wild-type and 29 *IP3R*[−] grommets from retina 1, and 15 wild type and 34 *IP3R*[−] from retina 2). Size averages from different retinas are indicated by circles of corresponding colors, and averages of different genotypes are indicated by black bars. **P*=0.008 (Student's *t*-test; *n*=2 retinas). (F) Schematic explanations of *vkg::GFP* morphology in various genotypes. In wild type, the pull by contracted stress fibers (red springs) enlarges the grommets and brings them closer together. In addition, the stress applied on ECM causes the materials between the grommets to crumple and form ridges. In contrast, as the contractile force is absent in *IP3R*[−] mutants, the grommets shrink in size and are farther apart, and the ECM ridges are diminished. In mosaic cluster, tensions are present on only one side of the cluster, resulting in an apparent shift of grommet position towards the *IP3R*⁺ side.

IOC waves. These observations imply that IOC waves are insulated from photoreceptor activities. Likewise, a mechanism must exist to compartmentalize the IOC and cone cell Ca^{2+} networks. One possible mechanism may involve a restricted propagation of second messenger required for Ca^{2+} increases. For instance, *Inx2* (*Innexin 2*), a *Drosophila* homolog of the gap junction component connexin, is expressed specifically in IOCs and localized to the endfeet (Richard and Hoch, 2015). As *Inx2* mediates the injury-induced slow Ca^{2+} waves in wing discs (Restrepo and Basler, 2016; Balaji et al., 2017), it may act similarly in the eye to regulate a cell-specific passage of second messenger required for IOC waves.

More importantly, using mutational analysis of *IP3R*, we have demonstrated involvement of Ca^{2+} communication in facilitating and coordinating stress fiber contraction at IOC endfeet. During pupal development, the appearance of endfeet stress fibers transitions from arrays of filaments emanating from the grommets at mid-pupal stage to large patches at late pupal stage (Baumann, 2004; Longley and Ready, 1995). The profiles of these structures continue to consolidate and appear as small dense patches by eclosion. In *IP3R*[−] adult and pupal mutant retinas, the morphology of stress fibers arrests at earlier stages. Concomitantly, the retinal floor in *IP3R*[−] clones increases by ~40%, consistent with the notion that stress fiber contraction powers the retinal floor condensation. The apical surface in *IP3R*[−] clones remains unaffected, suggesting that *IP3R*[−] does not disrupt actin cytoskeleton globally and its effect on endfeet stress fibers is specific. Collectively, these results indicate that *IP3R* has a role in facilitating the progression of stress fiber contraction at the endfeet. Interestingly, whole *IP3R*[−] eyes, generated by the *EGUF-GMR-hid* method (Stowers and Schwarz, 1999), appear larger and rounder (Bollepalli et al., 2017), in support of our observations that *IP3R* is linked to the formation of retinal curvature.

Several lines of evidence suggest that IOC waves and endfeet stress fiber contractions are causally linked. First, the phenomena of IOC waves and endfeet compaction are spatially and temporally correlated. Both processes are manifested in the secondary and tertiary pigment cells, and the emergence of IOC waves overlaps with the duration of endfeet stress fiber contraction. In addition, elimination of *IP3R* function in the eye does not affect cell fate determination and phototransduction (Acharya et al., 1997; Raghu et al., 2000), suggesting that these defects in IOC waves and stress fiber contractions are specific. Furthermore, MRLC Ser-19 phosphorylation at the retinal floor in *IP3R*[−] clones is reduced, supporting a plausible mechanism by which IOC waves regulate myosin II activity through modulation of MRLC phosphorylation. Based on these observations, we propose that the removal of *IP3R* function abolishes Ca^{2+} increase from internal stores, which directly disrupts the occurrence of IOC waves. The absence of cytosolic Ca^{2+} increase in IOCs then inactivates myosin II at the endfeet, thereby inhibiting stress fiber contraction and retinal floor condensation. As Ca^{2+} increases in IOCs are elicited by waves, the stress fiber contractions required for retinal floor morphogenesis are coordinated. Alternatively, cytoskeletal elements can alter the subcellular distribution of *IP3R* and impact Ca^{2+} signaling (Walker et al., 2002; Turvey et al., 2005; Hours and Mery, 2010), and it is possible that the interaction between the actomyosin network and *IP3R* in IOC endfeet contraction is more complex than we envision.

The consistency of Ca^{2+} spikes in IOC waves makes this cellular communication well suited for coordinating endfeet stress fiber contraction for floor condensation. Analysis of IOC Ca^{2+} spikes suggest the presence of a regular refractory period, which ensures that all IOCs of the same eye experience a similar number of spikes, regardless of the frequency of IOC wave initiations. Furthermore, no

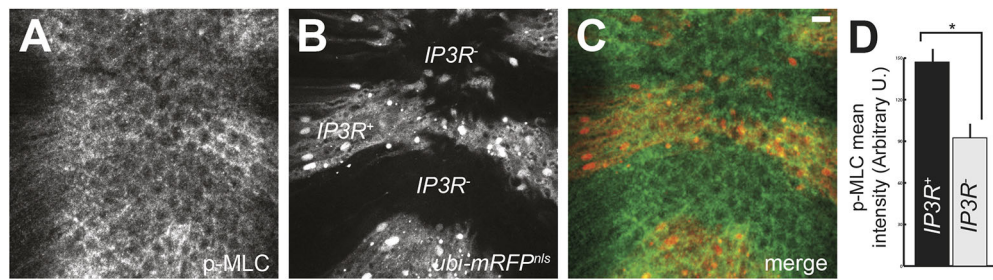


Fig. 9. Phosphorylated myosin regulatory light chain is reduced in $IP3R^-$ cells. (A–C) Maximum intensity projections of confocal sections of *ey-FLP; cn, bw; FRT^{82B}, l(3)itpr^{90B.0}/FRT^{82B}, ubi-mRFP^{nls}* retina stained with anti-phospho-MLC (A; green in C). The $IP3R^+$ and $IP3R^-$ patches are labeled by the presence and the absence of mRFP (B; red in C), respectively. Scale bar: 10 μ m. The staining is representative of images from two independent experiments. (D) Quantification of p-MLC mean intensities in $IP3R^+$ and $IP3R^-$ cells. * $P < 0.001$ (paired, two-tailed Student's *t*-test; $n = 6$).

increase in Ca^{2+} spike amplitude was seen in cells at wave merging, suggesting that all IOC waves experience Ca^{2+} spikes of similar amplitude. Indeed, we confirmed that IOC Ca^{2+} spike parameters from different regions of the eye were similar. It is possible that this uniformity of Ca^{2+} spikes in IOC waves ensure that the contractile forces are evenly applied across the retina during floor reduction. Ca^{2+} oscillations in cultured myofibroblasts have been shown to induce periodic micro-contractions of actin fibers (Castella et al., 2010), and it is likely that IOC waves have a similar effect on actin stress fibers at the pigment cell endfeet. In this scenario, regular passages of IOC waves would induce periodic and incremental contractions of the endfeet stress fibers to compact the retinal floor. Tensile forces driving the apical constriction of cells in the mesoderm furrow during gastrulation and pulling the epidermis cells to move dorsally during dorsal closure also occur in a pulsed fashion (Solon et al., 2009; Martin et al., 2009).

Although the floor area increase in $IP3R^-$ implicates IOC waves in floor condensation, the phenotypic severity (40%) is significantly less than the fourfold area reduction required (Longley and Ready, 1995), indicating that IOC wave-mediated contraction is not the sole mechanism for basal surface compaction. In support of this, the pupal retinal floor reduction commences at ~55% pupal development, earlier than the start of IOC wave formation. Thus, the retinal floor condensation consists of at least two phases: an early IOC wave-independent phase, which contributes to the majority of basement reduction, and a late IOC wave-dependent phase. We have observed mid-pupal retina containing clusters at different stages of floor reduction (Fig. S6D–F), implying that the condensation of ommatidial basement is initiated locally in patches and that the clusters in different patches may compact at different rates. Tensile forces coordinated by IOC waves during the late phase may fine-tune the floor condensation by smoothing out these differences from the early phase.

The retinal basement membrane, the ECM plane that defines the proximal surface of the retina, is organized into two specializations: grommets and ridges. Grommets, the exit ports through which photoreceptor axons leave the retina, first form in early pupae at the completion of pattern formation (Fig. S6A–C). Ridges, dense linear ECM between adjacent grommets, emerge as stress fiber contraction draws grommets together. In wild-type pupal eyes containing a mixture of fully and partially contracted stress fibers, ridges were prominent in regions with dense stress fibers (Fig. S6D–F, arrowheads). In $IP3R^-$ clones with reduced contraction, ridges were reduced. Together, these observations suggest that ridges are raised as compression deforms and buckles the ECM meshwork. Ridges assemble into a hexagonal network oriented orthogonally to the contractile stress fiber network. As Vkg

(collagen IV) stiffens ECM (Walma and Yamada, 2020), the ridge network may supply elastic energy that counterbalances the contractile forces, thereby maintaining a stable retinal floor. The fly eye should be an excellent model for investigating how stress fiber contractile forces and ECM dynamics cooperate to shape tissues.

MATERIALS AND METHODS

Drosophila genetics

All fly crosses were carried out at 25°C in standard laboratory conditions. *IGMR-GAL4* (8605), *UAS-GCaMP6m* (20XUAS-IVS-GCaMP6m; 42748), *norpA³⁶* (9048), *FRT^{82B}*, *GMR-src-mRFP* (7124), *FRT^{82B}*, *ubi-mRFP^{nls}* (30555) and *ey-GAL4*, *UAS-FLP*; *FRT^{82B}*, *GMR-hid/TM2* (5253) were obtained from Bloomington Stock Center (Bloomington stock numbers are indicated in parentheses). Both *IGMR-GAL4* and *UAS-GCaMP6m* have transgenic insertions on the 2nd and 3rd chromosomes, and we have generated *IGMR>GCaMP6m* recombinants for respective chromosomes. Both *IGMR>GCaMP6m* recombinants exhibited similar Ca^{2+} waves; nonetheless, for simplicity and consistency, we used the 2nd chromosome recombinant to generate all the movies presented. The *FRT^{82B}, l(3)itpr^{90B.0}* recombinant was a gift from Dr Roger Hardie (Cambridge University, UK), and the *vkg::GFP* (*GFP^{vkg-G00454}*) protein trap line (Morin, 2003) was a gift from Dr Wu-Min Deng (Tulane University School of Medicine, USA).

To monitor Ca^{2+} activities in $IP3R$ mitotic clones, *IGMR>GCaMP6m/CyO*; *FRT^{82B}, l(3)itpr^{90B.0}/TM3* males were mated with *ey-FLP/CyO*; *FRT^{82B}, GMR-src-mRFP/TM3* females. $IP3R$ clones in the adult eyes of *ey-FLP/IGMR>GCaMP6m*; *FRT^{82B}, l(3)itpr^{90B.0}/FRT^{82B}, GMR-src-mRFP* progeny, easily recognized by the absence of membrane-associated mRFP, were imaged as described below. To examine actin stress fiber morphology in $IP3R$ clones, *cn, bw*; *FRT^{82B}, l(3)itpr^{90B.0}/TM3* males were mated with *ey-FLP*; *cn, bw*; *FRT^{82B}, ubi-mRFP^{nls}/TM3* females. To monitor Vkg::GFP localization in $IP3R$ clones, *cn, bw*, *vkg::GFP*; *FRT^{82B}, l(3)itpr^{90B.0}/TM3* males were mated with *ey-FLP*; *cn, bw*, *vkg::GFP*; *FRT^{82B}, ubi-mRFP^{nls}/TM3* females. To generate $IP3R^-$ Vkg::GFP-containing retinas for western blotting, *cn, bw*, *vkg::GFP*; *FRT^{82B}, l(3)itpr^{90B.0}/TM3* or *cn, bw*, *vkg::GFP*; *FRT^{82B}* (control) males were mated with *ey-GAL4*, *UAS-FLP*; *FRT^{82B}, GMR-hid/TM2* females.

GCaMP6 imaging

For each Ca^{2+} activity recording, a live fly was glued eye-first onto a clean glass coverslip (Franceschini and Kirschfeld, 1971), maintained over an hour in the dark for adaptation, and exposed to 647 nm light pulses to shift active metarhodopsin to rhodopsin prior to imaging. Mounted flies were imaged on an inverted Nikon Eclipse TE2000 using a Nikon 40×1.3 Plan Fluor objective. Time-lapse movies were captured at one frame every 2 s, unless otherwise indicated, for 5 min using a Photometrics CoolSNAP camera controlled using Metamorph. Images were binned 2×2 and Nikon ND filters were used to attenuate excitation for typically 400 ms exposures. No decrease in signal was observed over single or repeated observations. Mounting is non-injurious to eyes and animals; when kept in a humid

chamber and fed with sugar water, it was possible to image flies repeatedly over several days.

For larval eye discs, tissues were dissected from crawling third instar larvae in their own hemolymph under a drop of halocarbon oil (Oil 10 S, VOLTAFLEF; VWR) on a coverslip. Coverslips were mounted on a microscope slide with spacers allowing full exposure of the halocarbon oil to air while imaging on the inverted Nikon microscope.

Imaging processing

The image files were rotated to bring anterior to the right and processed with ImageJ as described as below.

Sequential subtractions

Time-lapsed image stacks (2 s per frame for a 5-min recording) were separated into 151 individual png files using ImageJ (Image>Stacks>Stack to Images). A file series comprising sequential subtractions of signal intensities from consecutive png files were generated in Python (code provided upon request). Composite files with color-coded wave fronts from various time points are generated with ImageJ (Image>Color>Merge Channels). This operation was only performed on IOC recordings because the Ca^{2+} spike intervals in the cone cell movie (Movie 4) were too short.

Quantitative analysis of IOC GCaMP6m signals

To analyze the cellular signal intensities, the cells were labeled by hand in ImageJ with fixed-sized circular regions of interest (ROIs) (5-pixel diameter), which were imported into ROI manager. Text files containing the mean signal intensities over time were then generated with the Multi-Measure function, and the numeric series were processed by a Python code (code provided upon request). The code normalized the intensity values from each cell by subtracting the minimal value in the series and dividing by the range [i.e. $F_{\text{normalized}} = (F - F_{\text{min}}) / (F_{\text{max}} - F_{\text{min}})$]. With an artificial cutoff of 0.24 (the value was empirically determined from applying the algorithm on several data sets, and $F_{\text{normalized}} < 0.24$ is considered noise), the number of peaks, duration of peaks, intervals between peaks, time of onset for the peaks (T_{on}), and time to baseline return for the peaks (T_{off}) were counted.

Quantitative analysis of cone cell GCaMP6m signals

The cone cell movie (Movie 4) had significant sample movements, which interfered with the extraction of mean intensity over time in individual cells. This issue was remedied by digitally stabilizing the image frames with the ImageJ Template-Matching plug-in. To improve the image quality, a minimum z-stack projection was used as denominator for each frame with ImageJ Ratio Plus to make a ratio movie, followed by the ImageJ Enhance Contrast function. To characterize cone cell spikes, cells were manually labeled with fixed-sized circular ROIs and mean signal intensities over time were obtained with ImageJ as described for IOCs (see 'Quantitative analysis of IOC GCaMP6m signals'). However, because the signal intensities in cone cells were dim and often influenced by the passages of IOC waves, the cone cell signal intensities were normalized by subtracting the signal intensity from a nearby IOC.

Comparison of GCaMP6m in *IP3R*⁻ mosaic eye

For comparing GCaMP6m in *IP3R*⁻ mosaic eye, we obtained an mRFP map of the eye prior to the acquisition of a time-lapse stack of the GCaMP6m signal. A dual color movie of *IP3R*⁻ mosaic eye (Movie 9) was generated from 151 composite files, derived from merging individual GCaMP6m image files with the mRFP map file in ImageJ.

Immunostaining and western blot analysis

For immunostaining, dissected retinas were fixed with 4% paraformaldehyde and permeabilized with PBS+0.3% Triton X-100. Retinas were incubated with rabbit anti-phospho-MLC (3671T; SER-19; Cell Signaling Technology) polyclonal antibody at 1:10 overnight at 4°C and washed four times with PBS+0.3% Triton X-100. Alexa-conjugated phalloidin 647 (A22287, Invitrogen) and Alexa Fluor 488 secondary antibody (A11034, Invitrogen) were used at 1:100. All images were acquired with Zeiss LSM 710 laser-scanning confocal microscope. Zeiss Zen 2010 and Volocity (Improvision)

softwares were used to render confocal stacks for 3D reconstruction. To quantify phospho-MLC staining, six equal sized squares from wild-type and *IP3R*⁻ patches were randomly selected, and the mean signal intensities within these squares were determined with ImageJ.

For western blot analysis, 15 *cn*, *bw*, control, or *IP3R*⁻ heads, generated by *EGUF* method (Stowers and Schwarz, 1999), were homogenized in 50 µl 1× SDS loading buffer and boiled at 95°C for 5 min, then 8 µl samples were separated on 10% polyacrylamide gels, transferred onto Bio-Rad nitrocellulose membrane using semi-dry transfer (at 10 V for 45 min), and probed with rabbit polyclonal anti-GFP (ab6556, Abcam) or mouse monoclonal anti-β-tubulin (E7, Developmental Studies Hybridoma Bank, Iowa) antibodies at 1:1000 and 1:100, respectively. HRP-conjugated anti-rabbit (611-103-122, Rockland Immunochemicals) and anti-mouse (sc-2005, Santa Cruz Biotechnology) secondary antibodies were used at 1:10,000, and blots were developed using Luminol Chemiluminescent HRP Substrate (Thermo Scientific).

Acknowledgements

We thank Dr Roger Hardie (Cambridge University, UK) for sharing the *FRT*, *IP3R* recombinant and for discussion of *IP3R* phenotypes. Funding for the LSM710 was provided by a National Institutes of Health NCRR Shared Instrumentation Grant (1 S10 RR023734-01A1).

Competing interests

The authors declare no competing or financial interests.

Author contributions

Conceptualization: H.C.C., D.F.R.; Formal analysis: H.C.C., D.F.R.; Investigation: H.C.C., D.F.R.; Resources: H.C.C., D.F.R.; Writing - original draft: H.C.C., D.F.R.; Writing - review & editing: H.C.C., D.F.R.; Project administration: H.C.C., D.F.R.; Funding acquisition: H.C.C., D.F.R.

Funding

This work was supported by a Purdue Research Refresh Award from Purdue University (to H.C.C.) and the National Institutes of Health (EY 10306 to D.F.R.). Deposited in PMC for release after 12 months.

Peer review history

The peer review history is available online at <https://journals.biologists.com/dev/article-lookup/doi/10.1242/dev.199700>.

References

- Acharya, J. K., Jalink, K., Hardy, R. W., Hartenstein, V. and Zuker, C. S. (1997). InsP3 receptor is essential for growth and differentiation but not for vision in *Drosophila*. *Neuron* **18**, 881-887. doi:10.1016/S0896-6273(00)80328-1
- Akin, O., Bajar, B. T., Keles, M. F., Frye, M. A. and Zipursky, S. L. (2019). Cell-type-specific patterned stimulus-independent neuronal activity in the *Drosophila* visual system during synapse formation. *Neuron* **101**, 894-904.e5. doi:10.1016/j.neuron.2019.01.008
- Allaman, I., Bélanger, M. and Magistretti, P. J. (2011). Astrocyte-neuron metabolic relationships: for better and for worse. *Trends Neurosci.* **34**, 76-87. doi:10.1016/j.tins.2010.12.001
- Asteriti, S., Liu, C.-H. and Hardie, R. C. (2017). Calcium signalling in *Drosophila* photoreceptors measured with GCaMP6f. *Cell Calcium* **65**, 40-51. doi:10.1016/j.ceca.2017.02.006
- Balaji, R., Bielmeier, C., Harz, H., Bates, J., Stadler, C., Hildebrand, A. and Classen, A.-K. (2017). Calcium spikes, waves and oscillations in a large, patterned epithelial tissue. *Sci. Rep.* **7**, 42786. doi:10.1038/srep42786
- Barres, B. A. (2008). The mystery and magic of glia: a perspective on their roles in health and disease. *Neuron* **60**, 430-440. doi:10.1016/j.neuron.2008.10.013
- Baumann, O. (2004). Spatial pattern of nonmuscle myosin-II distribution during the development of the *Drosophila* compound eye and implications for retinal morphogenesis. *Dev. Biol.* **269**, 519-533. doi:10.1016/j.ydbio.2004.01.047
- Benlali, A., Draskovic, I., Hazelett, D. J. and Treisman, J. E. (2000). act up controls actin polymerization to alter cell shape and restrict Hedgehog signaling in the *Drosophila* eye disc. *Cell* **101**, 271-281. doi:10.1016/S0092-8674(00)80837-5
- Berridge, M. J., Lipp, P. and Bootman, M. D. (2000). The versatility and universality of calcium signalling. *Nat. Rev. Mol. Cell Biol.* **1**, 11-21. doi:10.1038/35036035
- Bloomquist, B. T., Shortridge, R. D., Schneuwly, S., Perdew, M., Montell, C., Steller, H., Rubin, G. and Pak, W. L. (1988). Isolation of a putative phospholipase C gene of *Drosophila*, *norpa*, and its role in phototransduction. *Cell* **54**, 723-733. doi:10.1016/S0092-8674(88)80017-5

- Bollepalli, M. K., Kuipers, M. E., Liu, C.-H., Asteriti, S. and Hardie, R. C.** (2017). Phototransduction in *Drosophila* is compromised by Gal4 expression but not by InsP3 receptor knockdown or mutation. *eNeuro* **4**, ENEURO.0143-17.2017. doi:10.1523/ENEURO.0143-17.2017
- Brito, C. and Sousa, S.** (2020). Non-Muscle Myosin 2A (NM2A): structure, regulation and function. *Cells* **9**, 1590. doi:10.3390/cells9071590
- Brodskiy, P. A., Wu, Q., Soundararajan, D. K., Huizar, F. J., Chen, J., Liang, P., Narciso, C., Levis, M. K., Arredondo-Walsh, N., Chen, D. Z. et al.** (2019). Decoding calcium signaling dynamics during *Drosophila* wing disc development. *Biophys. J.* **116**, 725-740. doi:10.1016/j.bpj.2019.01.007
- Brown, K. L., Cummings, C. F., Vanacore, R. M. and Hudson, B. G.** (2017). Building collagen IV smart scaffolds on the outside of cells. *Protein Sci.* **26**, 2151-2161. doi:10.1002/pro.3283
- Cagan, R. L. and Ready, D. F.** (1989). The emergence of order in the *Drosophila* pupal retina. *Dev. Biol.* **136**, 346-362. doi:10.1016/0012-1606(89)90261-3
- Castella, L. F., Buscemi, L., Godbout, C., Meister, J.-J. and Hinz, B.** (2010). A new lock-step mechanism of matrix remodelling based on subcellular contractile events. *J. Cell Sci.* **123**, 1751-1760. doi:10.1242/jcs.066795
- Chang, H. C., Newmyer, S. L., Hull, M. J., Ebersold, M., Schmid, S. L. and Mellman, I.** (2002). Hsc70 is required for endocytosis and clathrin function in *Drosophila*. *J. Cell Biol.* **159**, 477-487. doi:10.1083/jcb.200205086
- Chen, T.-W., Wardill, T. J., Sun, Y., Pulver, S. R., Renninger, S. L., Baohan, A., Schreiter, E. R., Kerr, R. B., Jayaraman, V. et al.** (2013). Ultrasensitive fluorescent proteins for imaging neuronal activity. *Nature* **499**, 295-300. doi:10.1038/nature12354
- Choi, B. J., Chen, Y.-C. D. and Desplan, C.** (2021). Building a circuit through correlated spontaneous neuronal activity in the developing vertebrate and invertebrate visual systems. *Genes Dev.* **35**, 677-691. doi:10.1101/gad.348241.121
- Cornell-Bell, A. H., Finkbeiner, S. M., Cooper, M. S. and Smith, S. J.** (1990). Glutamate induces calcium waves in cultured astrocytes: long-range glial signaling. *Science* **247**, 470-473. doi:10.1126/science.1967852
- Fernandes, V. M., McCormack, K., Lewellyn, L. and Verheyen, E. M.** (2014). Integrins regulate apical constriction via microtubule stabilization in the *Drosophila* eye disc epithelium. *Cell Rep.* **9**, 2043-2055. doi:10.1016/j.celrep.2014.11.041
- Fidler, A. L., Darris, C. E., Chetyrkin, S. V., Pedchenko, V. K., Boudko, S. P., Brown, K. L., Gray Jerome, W., Hudson, J. K., Rokas, A. and Hudson, B. G.** (2017). Collagen IV and basement membrane at the evolutionary dawn of metazoan tissues. *eLife* **6**, e24176. doi:10.7554/eLife.24176
- Fields, R. D. and Stevens-Graham, B.** (2002). New insights into neuron-glia communication. *Science* **298**, 556-562. doi:10.1126/science.298.5593.556
- Franceschini, N. and Kirschfeld, K.** (1971). [In vivo optical study of photoreceptor elements in the compound eye of *Drosophila*]. *Kybernetik* **8**, 1-13. doi:10.1007/BF00270828
- Freeman, M.** (1996). Reiterative use of the EGF receptor triggers differentiation of all cell types in the *Drosophila* eye. *Cell* **87**, 651-660. doi:10.1016/S0092-8674(00)81385-9
- Galy, A., Schenck, A., Sahin, H. B., Qurashi, A., Sahel, J.-A., Diebold, C. and Giangrande, A.** (2011). CYFIP dependent actin remodeling controls specific aspects of *Drosophila* eye morphogenesis. *Dev. Biol.* **359**, 37-46. doi:10.1016/j.ydbio.2011.08.009
- Guillot, C. and Lecuit, T.** (2013). Mechanics of epithelial tissue homeostasis and morphogenesis. *Science* **340**, 1185-1189. doi:10.1126/science.1235249
- Halassa, M. M. and Haydon, P. G.** (2010). Integrated brain circuits: astrocytic networks modulate neuronal activity and behavior. *Annu. Rev. Physiol.* **72**, 335-355. doi:10.1146/annurev-physiol-021909-135843
- Hardie, R. C.** (1996). INDO-1 measurements of absolute resting and light-induced Ca^{2+} concentration in *Drosophila* photoreceptors. *J. Neurosci.* **16**, 2924-2933. doi:10.1523/JNEUROSCI.16-09-02924.1996
- Heisenberg, C.-P. and Bellaïche, Y.** (2013). Forces in tissue morphogenesis and patterning. *Cell* **153**, 948-962. doi:10.1016/j.cell.2013.05.008
- Heissler, S. M. and Sellers, J. R.** (2016). Various themes of myosin regulation. *J. Mol. Biol.* **428**, 1927-1946. doi:10.1016/j.jmb.2016.01.022
- Homolya, L., Steinberg, T. H. and Boucher, R. C.** (2000). Cell to cell communication in response to mechanical stress via bilateral release of ATP and UTP in polarized epithelia. *J. Cell Biol.* **150**, 1349-1360. doi:10.1083/jcb.150.6.1349
- Hours, M. C. and Mery, L.** (2010). The N-terminal domain of the type 1 Ins(1,4,5)P₃ receptor stably expressed in MDCK cells interacts with myosin IIA and alters epithelial cell morphology. *J. Cell Sci.* **123**, 1449-1459. doi:10.1242/jcs.057687
- Jaffe, L. F.** (2008). Calcium waves. *Philos. Trans. R. Soc. Lond. B Biol. Sci.* **363**, 1311-1316. doi:10.1098/rstb.2007.2249
- Kaneuchi, T., Sartain, C. V., Takeo, S., Horner, V. L., Buehner, N. A., Aigaki, T. and Wolfner, M. F.** (2015). Calcium waves occur as *Drosophila* oocytes activate. *Proc. Natl. Acad. Sci. USA* **112**, 791-796. doi:10.1073/pnas.1420589112
- Kefalides, N. A.** (1973). Structure and biosynthesis of basement membranes. *Int. Rev. Connect. Tissue Res.* **6**, 63-104. doi:10.1016/B978-0-12-363706-2.50008-8
- Kelso, R. J., Buszczak, M., Quinones, A. T., Castiblanco, C., Mazzalupo, S. and Cooley, L.** (2004). Flytrap, a database documenting a GFP protein-trap insertion screen in *Drosophila melanogaster*. *Nucleic Acids Res.* **32**, D418-D420. doi:10.1093/nar/gkh014
- Kramer, J. M. and Staveley, B. E.** (2003). GAL4 causes developmental defects and apoptosis when expressed in the developing eye of *Drosophila melanogaster*. *Genet. Mol. Res.* **2**, 43-47.
- Kurth-Nelson, Z. L., Mishra, A. and Newman, E. A.** (2009). Spontaneous Glial calcium waves in the retina develop over early adulthood. *J. Neurosci.* **29**, 11339-11346. doi:10.1523/JNEUROSCI.2493-09.2009
- Lee, A. and Treisman, J. E.** (2004). Excessive Myosin activity in mbs mutants causes photoreceptor movement out of the *Drosophila* eye disc epithelium. *Mol. Biol. Cell* **15**, 3285-3295. doi:10.1091/mbc.e04-01-0057
- Longley, R. L., Jr and Ready, D. F.** (1995). Integrins and the development of three-dimensional structure in the *Drosophila* compound eye. *Dev. Biol.* **171**, 415-433. doi:10.1006/dbio.1995.1292
- Lord, S. J., Velle, K. B., Mullins, R. D. and Fritz-Laylin, L. K.** (2020). SuperPlots: communicating reproducibility and variability in cell biology. *J. Cell Biol.* **219**, e202001064. doi:10.1083/jcb.202001064
- Martin, A. C., Kaschube, M. and Wieschaus, E. F.** (2009). Pulsed contractions of an actin-myosin network drive apical constriction. *Nature* **457**, 495-499. doi:10.1038/nature07522
- Morin, X.** (2003). In vivo protein trapping in *Drosophila*. *Brief. Funct. Genomic. Proteomic.* **2**, 137-141. doi:10.1093/bfpg/2.2.137
- Narciso, C. E., Contento, N. M., Storey, T. J., Hoelzle, D. J. and Zartman, J. J.** (2017). Release of applied mechanical loading stimulates intercellular calcium waves in *Drosophila* wing discs. *Biophys. J.* **113**, 491-501. doi:10.1016/j.bpj.2017.05.051
- Nie, J., Mahato, S. and Zelfhof, A. C.** (2014). The actomyosin machinery is required for *Drosophila* retinal lumen formation. *PLoS Genet.* **10**, e1004608. doi:10.1371/journal.pgen.1004608
- O'tousa, J. E.** (2002). Ca^{2+} regulation of *Drosophila* phototransduction. *Adv. Exp. Med. Biol.* **514**, 493-505. doi:10.1007/978-1-4615-0121-3_30
- Paluch, E. and Heisenberg, C.-P.** (2009). Biology and physics of cell shape changes in development. *Curr. Biol.* **19**, R790-R799. doi:10.1016/j.cub.2009.07.029
- Pearn, M. T., Randall, L. L., Shortridge, R. D., Burg, M. G. and Pak, W. L.** (1996). Molecular, biochemical, and electrophysiological characterization of *Drosophila* norpA mutants. *J. Biol. Chem.* **271**, 4937-4945. doi:10.1074/jbc.271.9.4937
- Raghu, P., Colley, N. J., Webel, R., James, T., Hasan, G., Danin, M., Selinger, Z. and Hardie, R. C.** (2000). Normal phototransduction in *Drosophila* photoreceptors lacking an InsP₃ receptor gene. *Mol. Cell. Neurosci.* **15**, 429-445. doi:10.1006/mcne.2000.0846
- Raghu, P., Coessens, E., Manifava, M., Georgiev, P., Pettitt, T., Wood, E., Garcia-Murillas, I., Okkenhaug, H., Trivedi, D., Zhang, Q. et al.** (2009). Rhabdome biogenesis in *Drosophila* photoreceptors is acutely sensitive to phosphatidic acid levels. *J. Cell Biol.* **185**, 129-145. doi:10.1083/jcb.200807027
- Restrepo, S. and Basler, K.** (2016). *Drosophila* wing imaginal discs respond to mechanical injury via slow InsP₃-mediated intercellular calcium waves. *Nat. Commun.* **7**, 12450. doi:10.1038/ncomms12450
- Richard, M. and Hoch, M.** (2015). *Drosophila* eye size is determined by Innexin 2-dependent Decapentaplegic signalling. *Dev. Biol.* **408**, 26-40. doi:10.1016/j.ydbio.2015.10.011
- Roignant, J.-Y. and Treisman, J. E.** (2009). Pattern formation in the *Drosophila* eye disc. *Int. J. Dev. Biol.* **53**, 795-804. doi:10.1387/ijdb.072483jr
- Scemes, E. and Giaume, C.** (2006). Astrocyte calcium waves: what they are and what they do. *Glia* **54**, 716-725. doi:10.1002/glia.20374
- Scholey, J. M., Taylor, K. A. and Kendrick-Jones, J.** (1980). Regulation of non-muscle myosin assembly by calmodulin-dependent light chain kinase. *Nature* **287**, 233-235. doi:10.1038/287233a0
- Solon, J., Kaya-Çopur, A., Colombelli, J. and Brunner, D.** (2009). Pulsed forces timed by a ratchet-like mechanism drive directed tissue movement during dorsal closure. *Cell* **137**, 1331-1342. doi:10.1016/j.cell.2009.03.050
- Stowers, R. S. and Schwarz, T. L.** (1999). A genetic method for generating *Drosophila* eyes composed exclusively of mitotic clones of a single genotype. *Genetics* **152**, 1631-1639. doi:10.1093/genetics/152.4.1631
- Takeuchi, Y., Narumi, R., Akiyama, R., Vitiello, E., Shirai, T., Tanimura, N., Kuromiya, K., Ishikawa, S., Kajita, M., Tada, M. et al.** (2020). Calcium wave promotes cell extrusion. *Curr. Biol.* **30**, 670-681.e6. doi:10.1016/j.cub.2019.11.089
- Tsachaki, M. and Sprecher, S. G.** (2012). Genetic and developmental mechanisms underlying the formation of the *Drosophila* compound eye. *Dev. Dyn.* **241**, 40-56. doi:10.1002/dvdy.22738
- Turvey, M. R., Fogarty, K. E. and Thorn, P.** (2005). Inositol (1,4,5)-trisphosphate receptor links to filamentous actin are important for generating local Ca^{2+} signals in pancreatic acinar cells. *J. Cell Sci.* **118**, 971-980. doi:10.1242/jcs.01693
- Venkatesh, K. and Hasan, G.** (1997). Disruption of the IP₃ receptor gene of *Drosophila* affects larval metamorphosis and ecdysone release. *Curr. Biol.* **7**, 500-509. doi:10.1016/S0960-9822(06)00221-1
- Voolstra, O. and Huber, A.** (2020). Ca^{2+} signaling in *Drosophila* photoreceptor cells. *Adv. Exp. Med. Biol.* **1131**, 857-879. doi:10.1007/978-3-030-12457-1_34
- Waddington, C. H.** (1962). *New Patterns in Genetics and Development*. New York: Columbia University Press.

- Walker, D. S., Ly, S., Lockwood, K. C. and Baylis, H. A.** (2002). A direct interaction between IP(3) receptors and myosin II regulates IP(3) signaling in *C. elegans*. *Curr. Biol.* **12**, 951-956. doi:10.1016/S0960-9822(02)00868-0
- Walma, D. A. C. and Yamada, K. M.** (2020). The extracellular matrix in development. *Development* **147**, dev175596. doi:10.1242/dev.175596
- Warner, S. J. and Longmore, G. D.** (2009a). Cdc42 antagonizes Rho1 activity at adherens junctions to limit epithelial cell apical tension. *J. Cell Biol.* **187**, 119-133. doi:10.1083/jcb.200906047
- Warner, S. J. and Longmore, G. D.** (2009b). Distinct functions for Rho1 in maintaining adherens junctions and apical tension in remodeling epithelia. *J. Cell Biol.* **185**, 1111-1125. doi:10.1083/jcb.200901029
- Wernet, M. F., Labhart, T., Baumann, F., Mazzoni, E. O., Pichaud, F. and Desplan, C.** (2003). Homothorax switches function of *Drosophila* photoreceptors from color to polarized light sensors. *Cell* **115**, 267-279. doi:10.1016/S0092-8674(03)00848-1
- Wolff, T. and Ready, D. F.** (1991). The beginning of pattern formation in the *Drosophila* compound eye: the morphogenetic furrow and the second mitotic wave. *Development* **113**, 841-850. doi:10.1242/dev.113.3.841
- Yasothornsrikul, S., Davis, W. J., Cramer, G., Kimbrell, D. A. and Dearolf, C. R.** (1997). viking: identification and characterization of a second type IV collagen in *Drosophila*. *Gene* **198**, 17-25. doi:10.1016/S0378-1119(97)00274-6
- York-Andersen, A. H., Parton, R. M., Bi, C. J., Bromley, C. L., Davis, I. and Weil, T. T.** (2015). A single and rapid calcium wave at egg activation in *Drosophila*. *Biol. Open* **4**, 553-560. doi:10.1242/bio.201411296
- York-Andersen, A. H., Hu, Q., Wood, B. W., Wolfner, M. F. and Weil, T. T.** (2020). A calcium-mediated actin redistribution at egg activation in *Drosophila*. *Mol. Reprod. Dev.* **87**, 293-304. doi:10.1002/mrd.23311

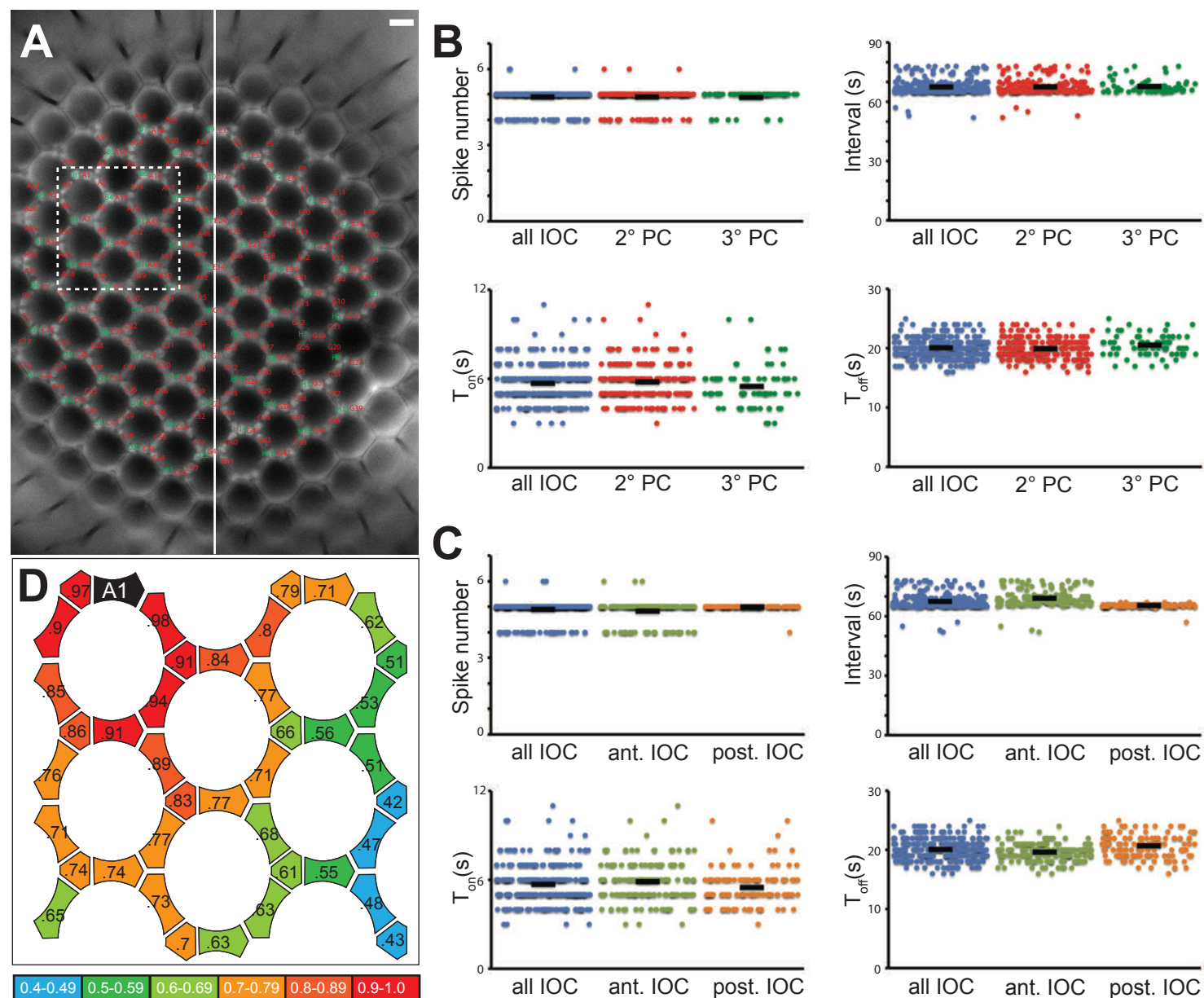


Fig. S1. IOC Ca^{2+} transients are similar across the retina. (A) A micrograph of *IGMR>GCaMP6/+* retina showing secondary (green) and tertiary (red) pigment cells labeled for quantitative analysis. A white line artificially demarcates the anterior and posterior halves. Scale bar=10 μ m. (B) Scatter plots of spike characteristics from IOCs (n=273 cells, blue dots), secondary (n=204 cells, red dots), and tertiary (n=69 cells, green dots) pigment cells from this recording. Dots represent the numbers (spike numbers, interval averages, and T_{ON} and T_{OFF} averages) obtained from individual cells, and averages from cell populations are indicated by black bars. (C) Comparison of IOC Ca^{2+} spike parameters from the anterior (n=118 cells, light green dots) and posterior (n=155 cells, orange dots) halves. Averages from different halves are indicated by black bars. (D) A schematic map showing pair-wise Pearson correlation analysis performed on numeric series generated from GCaMP6m intensities over time with cell A1. Region containing analyzed clusters corresponds to the dashed box in A. The cells closest to A1 exhibit higher correlations than those farther away.

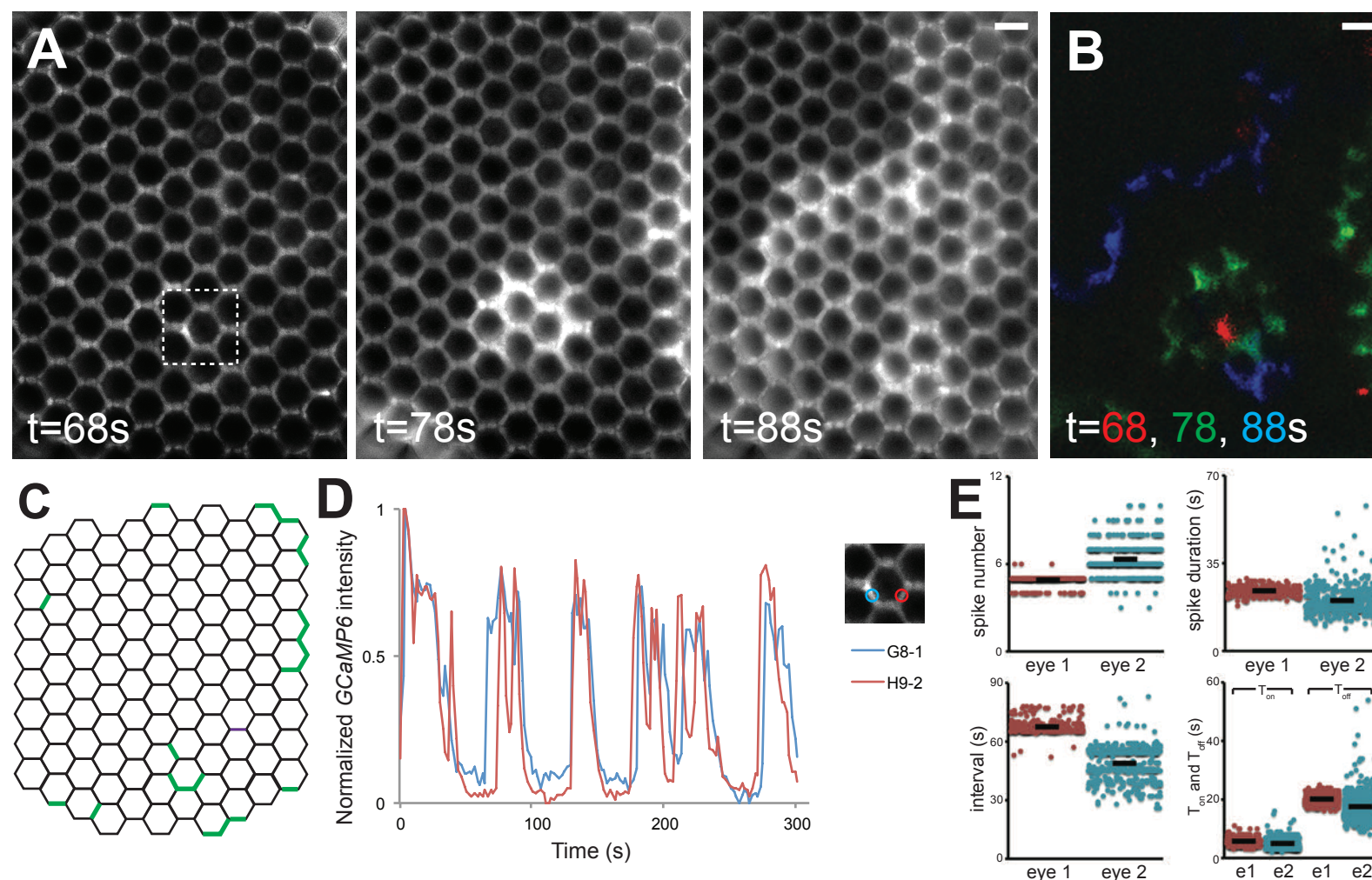


Fig. S2. Comparison of IOC waves from two independent eyes. (A) A micrograph montage of 10s intervals showing a Ca^{2+} wave initiated in the ventral region (dashed box) of a young *IGMR>GCaMP6m* retina at t=68s. Scale bar=10 μm . (B) An image overlaying three wave fronts at t=68s (red), 78s (green), and 88s (blue) respectively. This IOC wave is the same one shown in A. At t=78 sec, a distinct wave front approaches from the anterior edge. (C) A schematic representation of the IOC wave origins, each denoted with a green line. Comparing to the movie shown in Fig. 2, this recording is noisier with more “flickering”, and only those resulted in waves are indicated. (D) Plot of normalized GCaMP6m intensity $((F-F_{\text{min}})/(F_{\text{max}}-F_{\text{min}}))$ over time showing the regular Ca^{2+} oscillation in 2 secondary pigments cells (G8-1 and H9-2), selected from the dashed box in A. (E) Scatter plots comparing IOC Ca^{2+} spike characteristics from two independent young *IGMR>GCaMP6m* retinas. Eye 1 corresponds to the retina shown in Fig. 2 (n=273 cells, dark red dots) and Eye 2 (n=474 cells, light blue dots) is the retina shown in this figure. Dots represent the numbers from individual cells, and averages from IOCs of different eyes are indicated by black bars.

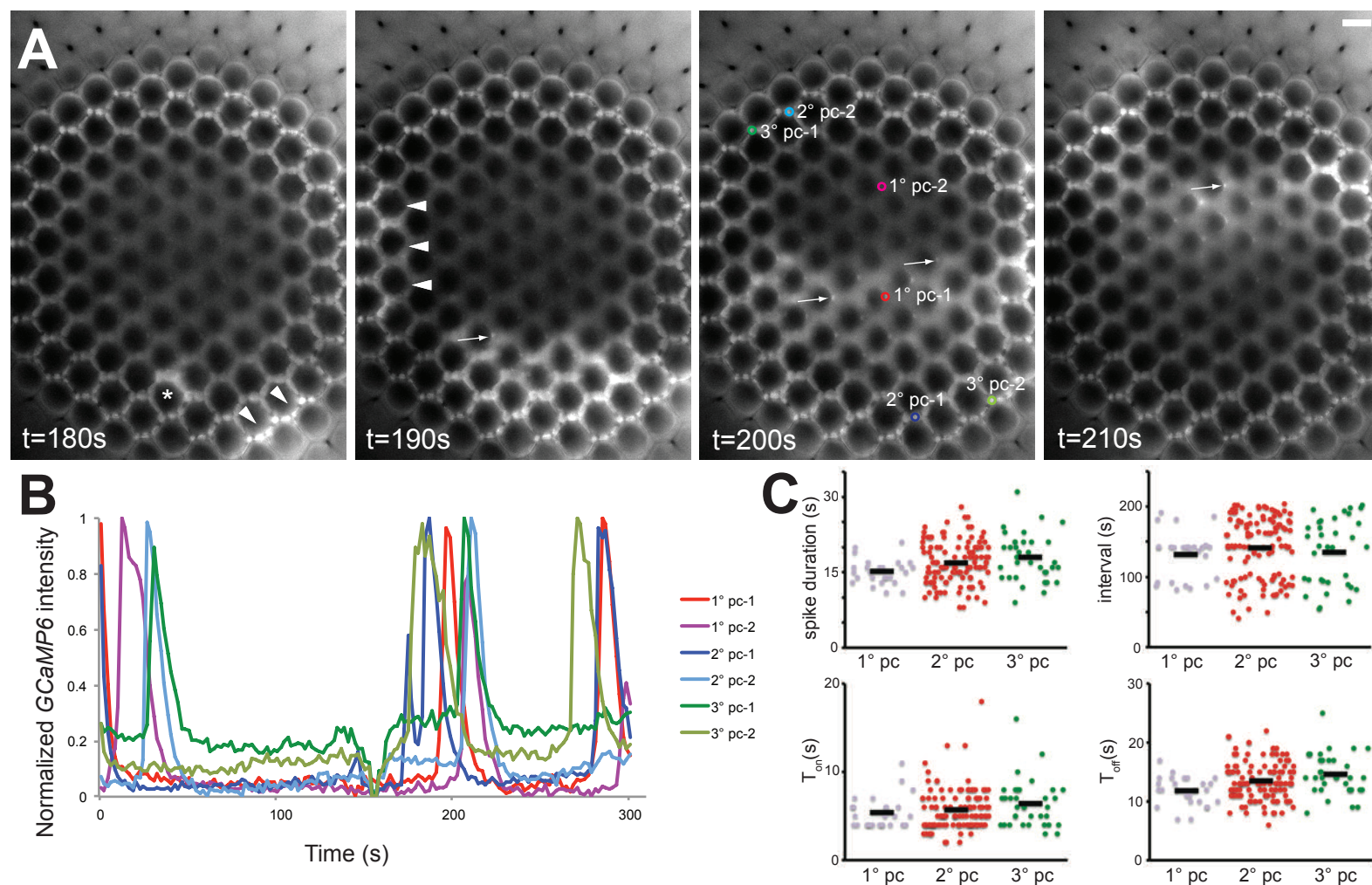


Fig. S3. IOC waves propagate through primary, secondary, and tertiary pigment cells. (A) A young adult retina showing *GCaMP6m* signals from all three pigment cell types in different regions of the eye. Because of the retinal curvature, Ca²⁺ transients from secondary and tertiary pigment cells are readily recognized around the retinal periphery, whereas signals from the nuclei of anterior primary pigment cells in the central region are seen (arrows). In primary pigment cells, *GCaMP6m* signals in the nuclei are more prominent because of the quenching of cytoplasmic *GCaMP6m* fluorescence by pigment granules. The nuclei from the posterior primary pigment cells are not visible due to the angle of specimen preparation. At t=180s, wave initiations were seen at the anterior-ventral edge (arrowheads) and in nearby internal IOC cells (asterisk). At t=190s, another wave front was seen at the posterior edge (arrowheads). These waves then merged and moved dorsally across the *GCaMP6m* retina through all three pigment cell types. (B) Plot of normalized *GCaMP6m* intensity ($(F - F_{min}) / (F_{max} - F_{min})$) over time showing the Ca²⁺ oscillation in two primary (red and magenta lines), two secondary (blue and light blue), and two tertiary (green and light green) cells. The line colors correspond to color circles (selected cells) in A. The dip in *GCaMP6m* intensity around t=160s was caused by a sudden movement of the specimen. (C) Scatter plots comparing spike characteristics (duration, interval, T_{on}, and T_{off}) between primary (n=26 cells, gray dots), secondary (n=115 cells, red dots), and tertiary (n=35 cells, green dots) pigment cells of this recording. Averages of different cell types are indicated by black bars.

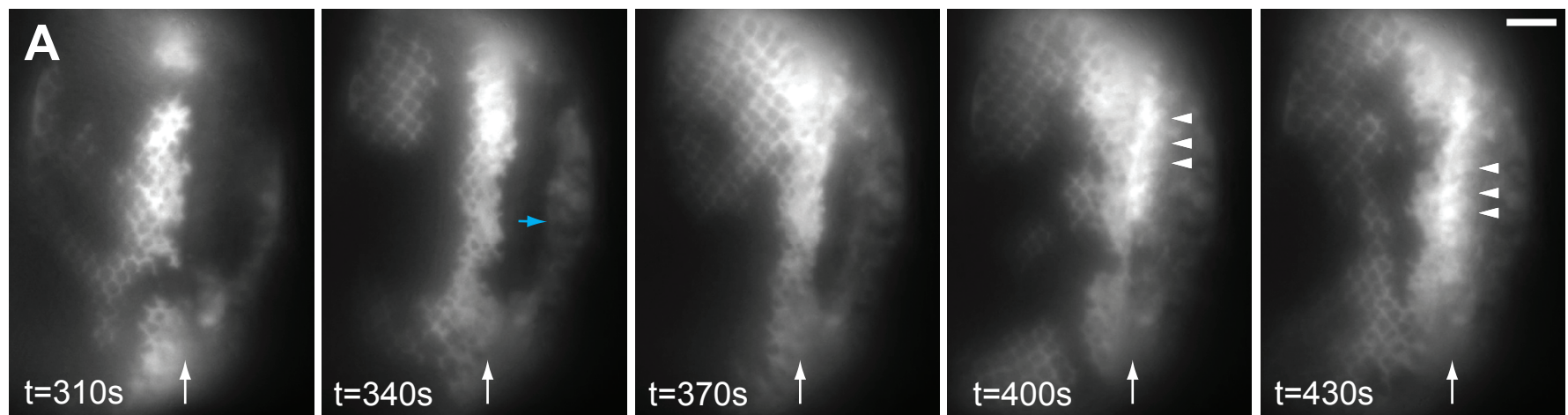


Fig. S4. Ca^{2+} waves are present in larval eye discs. (A) A micrograph montage of an *ey-GAL4; UAS-GCaMP6m* eye disc in 30s intervals, showing the presence of Ca^{2+} waves behind and ahead of the furrow (arrows). Instead of *IGMR-GAL4*, the larval eye disc was recorded with *ey-GAL4* to detect Ca^{2+} activities in cells anterior and posterior to the furrow. Ahead of the furrow, Ca^{2+} waves are present, but less frequent, and an example is shown initiating from the anterior edge at t=340s (blue arrow), reaching the furrow at ~400s. At the furrow, when cells experience Ca^{2+} spikes, high GCaMP6m signals are seen in regularly spaced cell clusters (arrowheads). Posterior to the furrow, Ca^{2+} waves are frequent with higher GCaMP6m signals in pre-LOCs, resulting in a honeycomb-like appearance. Scale bar=40 μm .

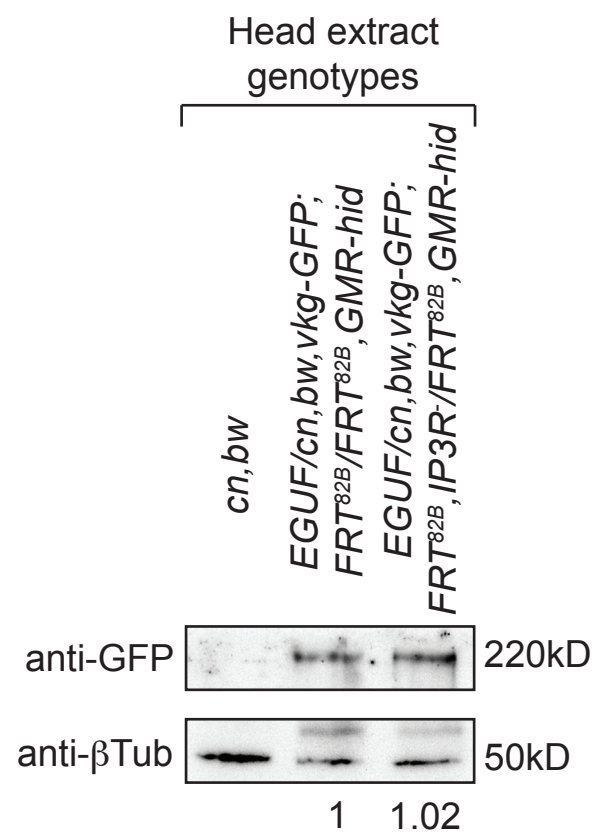


Fig. S5. vkg synthesis is unaffected in *IP3R* retina. Western blot of total head lysates from *cn, bw* (lane 1), *ey-GAL4, UAS-FLP/vkg::GFP; FRT^{82B}/FRT^{82B}, GMR-hid* (lane 2), and *ey-GAL4, UAS-FLP/vkg::GFP; FRT^{82B}, I(3)itpr^{90B.0}/FRT^{82B}, GMR-hid* (lane 3). The *vkg::GFP* proteins, absent in *cn, bw* extract, are detected by anti-GFP antibody, and the β -tubulin bands serve as loading controls. The GFP/ β -tubulin band intensity ratios are determined with ImageJ.

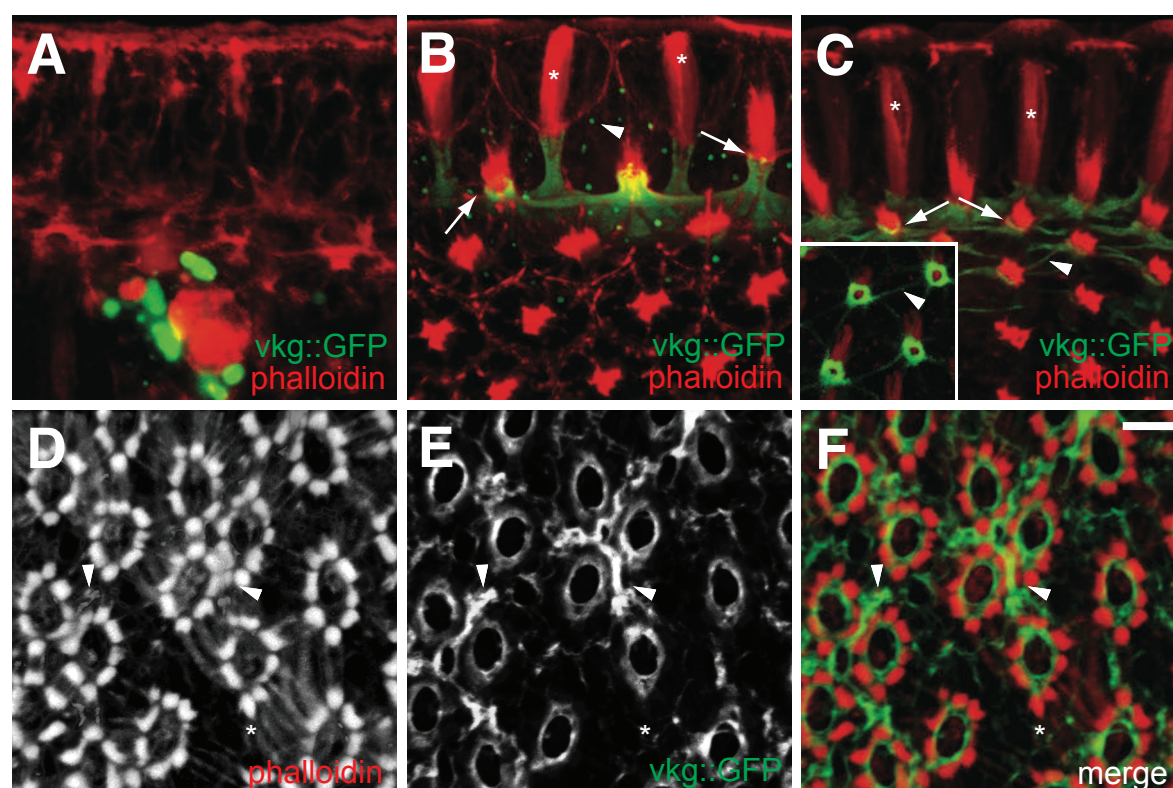
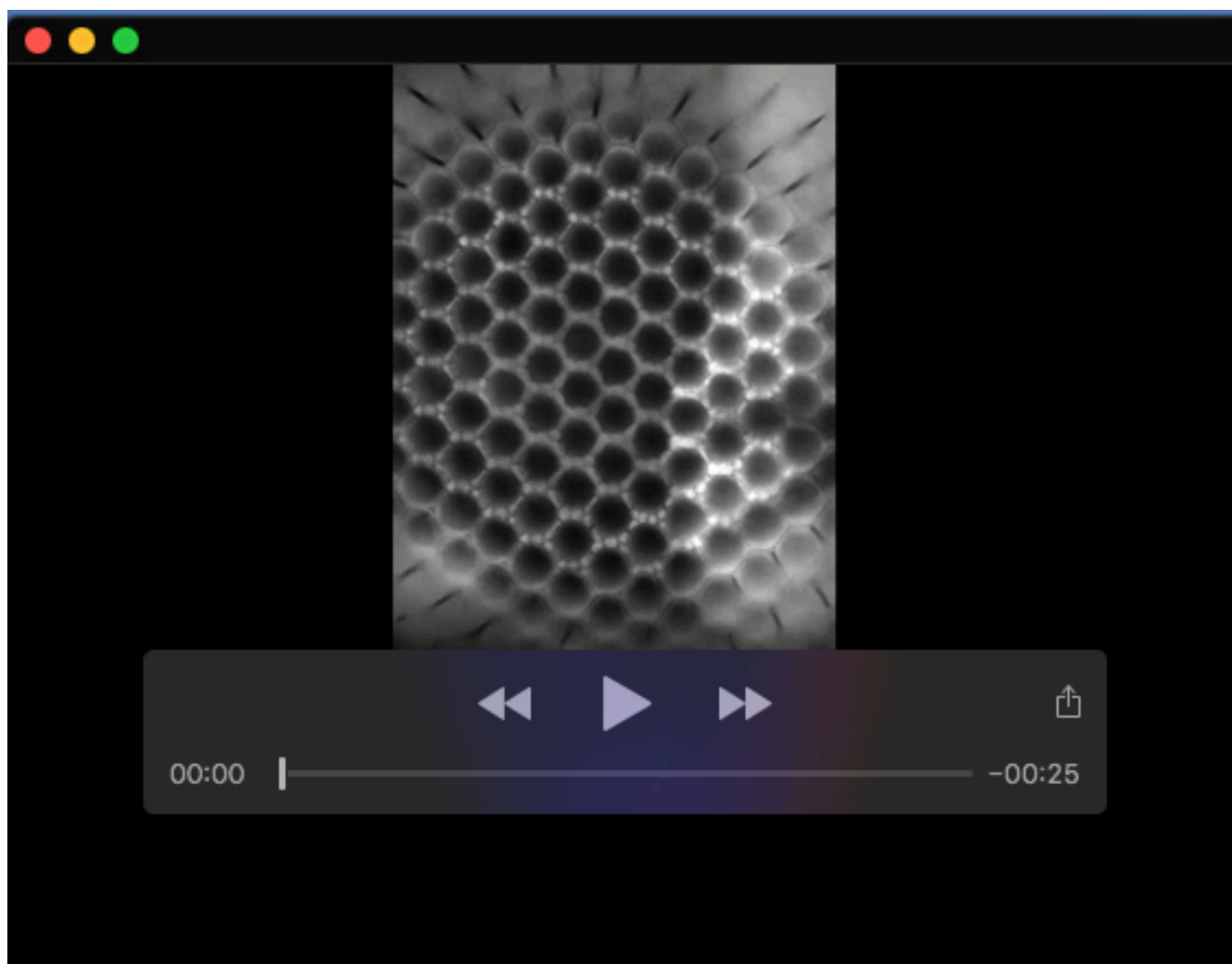
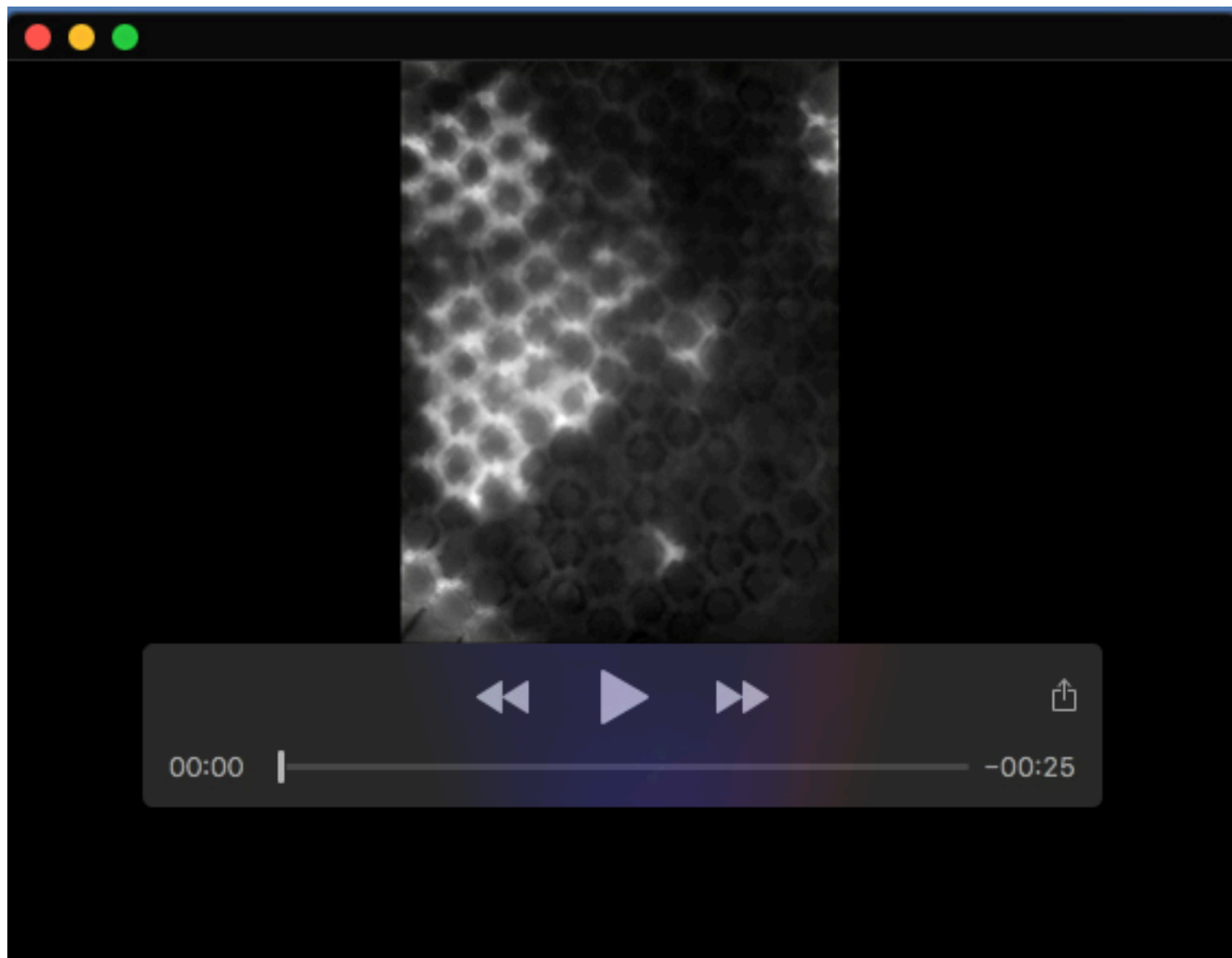


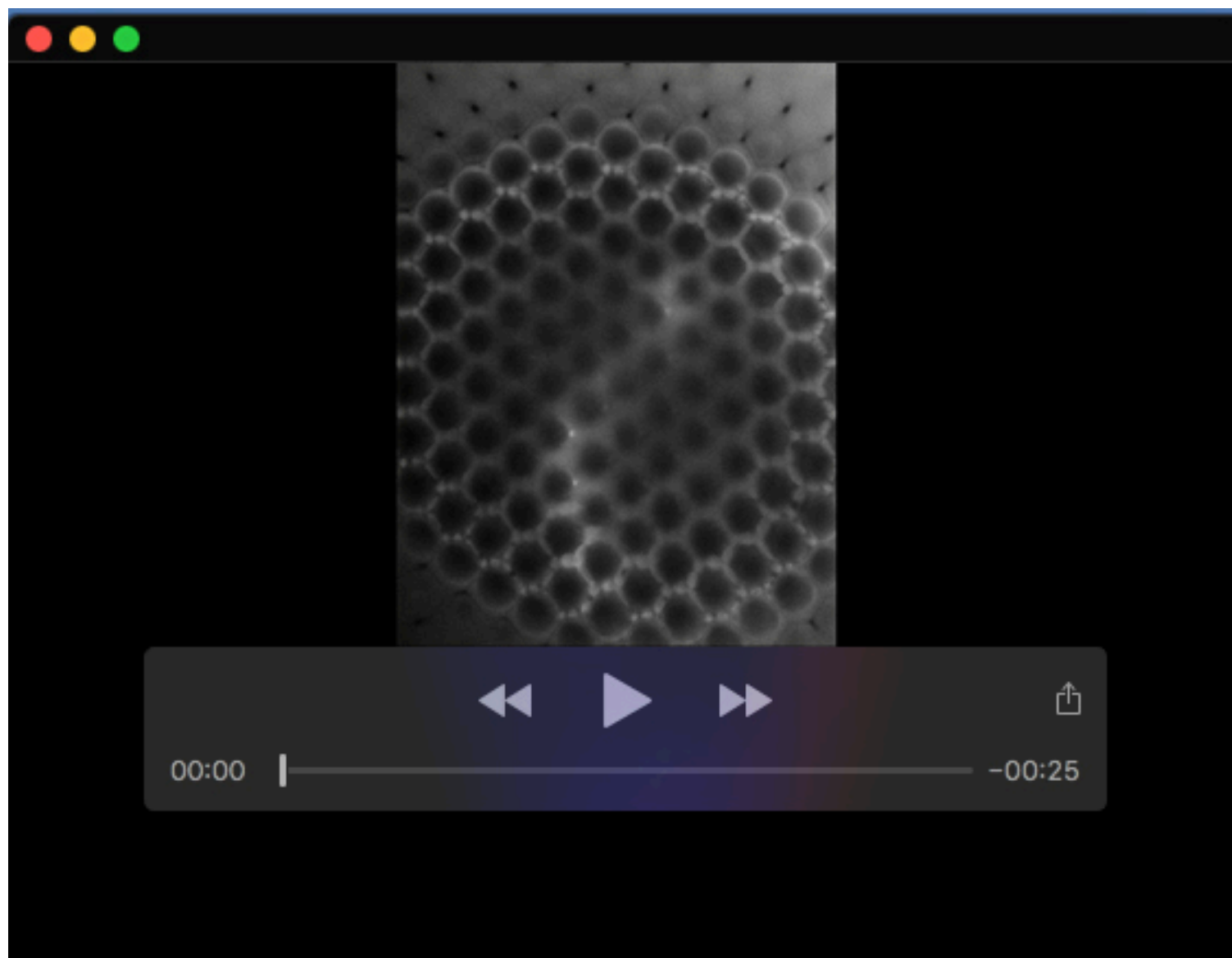
Fig. S6. The formation of grommets and ridges during pupal development. A-F) Snapshots of 3D rendering of confocal sections of *cn*, *bw*, *vkg::GFP* pupal retinas stained with phalloidin (red). (A) Prior to rhabdomere extension (at ~30% pupal development), unorganized vkg-positive structures are seen underneath the retina. (B) As the rhabdomeres (asterisks) are in the midst of extending throughout the depth of the retina (at ~45% pupal development), vkg-positive cylindrical structures rise from the basement membrane to interface with the growing rhabdomeres. At this stage, the photoreceptor cell cortex, revealed by phalloidin staining, and vkg-positive cylinder assume the appearance of a wineglass (with photoreceptor cell cortex being the “bowl” and vkg cylinder being the “stem”). The junctures between the rhabdomeres and vkg::GFP stems constitute the future grommets (arrows). In addition, vkg-positive puncta are seen inside the IOCs (arrowheads), suggesting that these cells deposit the ECM into the basement membrane. (C) At the completion of rhabdomere extension (at ~60% pupal development), elevated vkg::GFP signal labels the grommets (arrows, inset) and the IOC basal cell contacts at the retinal floor (arrowheads). A bottom view of a pupal eye at a similar stage as in (C) is shown in the inset. (D-F) At a later stage, the presence of vkg ridges correlates with the extent of actin stress fiber contraction, which varies across this retina. In regions where the stress fibers have contracted, the vkg ridges are prominent (arrowhead). In contrast, vkg ridges are reduced in regions where the stress fibers are extended (asterisk). Scale bar=10µm.



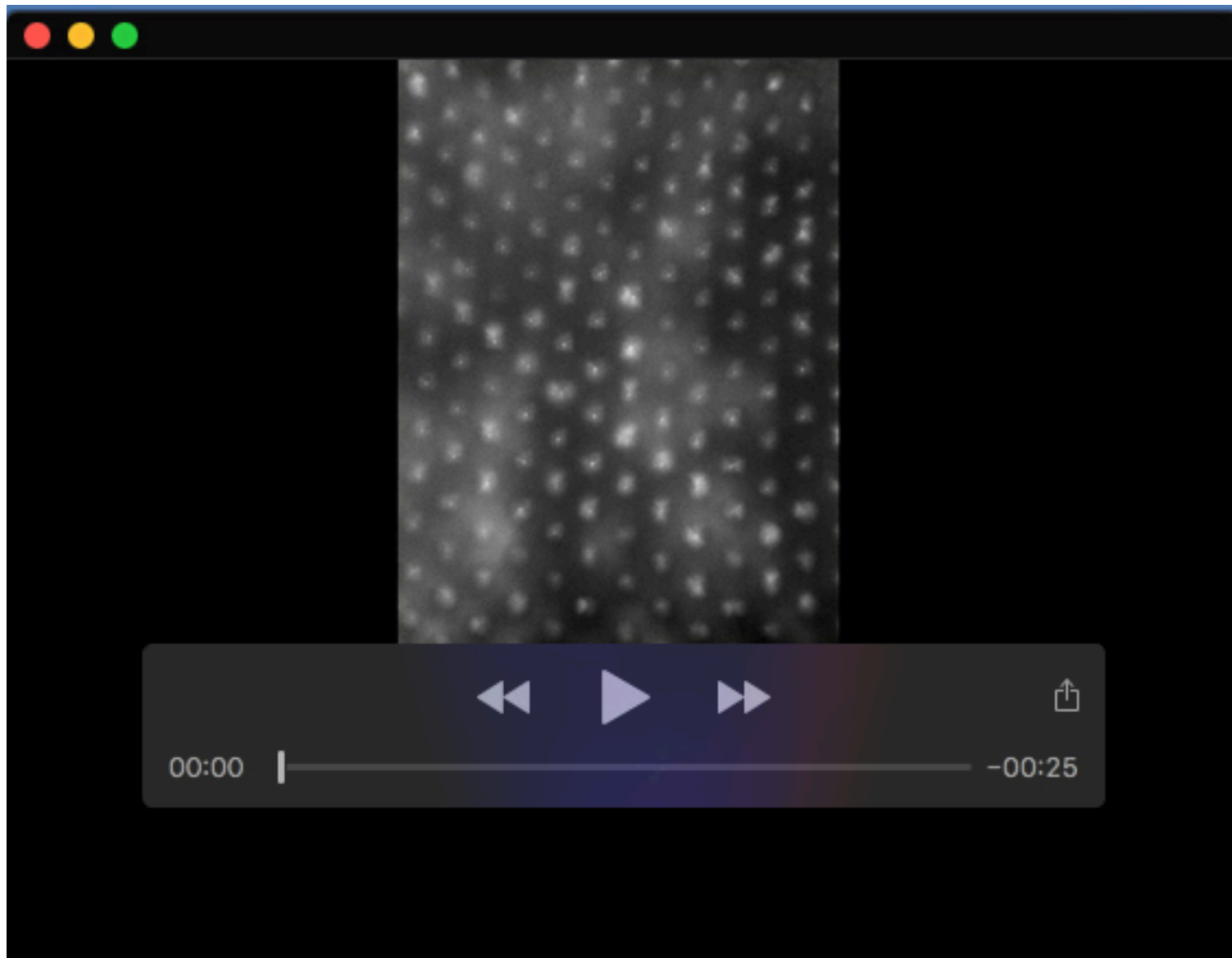
Movie 1. Young *IGMR>GCaMP6m/+* adult retina at a distal plane (Fig. 2), revealing Ca^{2+} waves in IOCs.



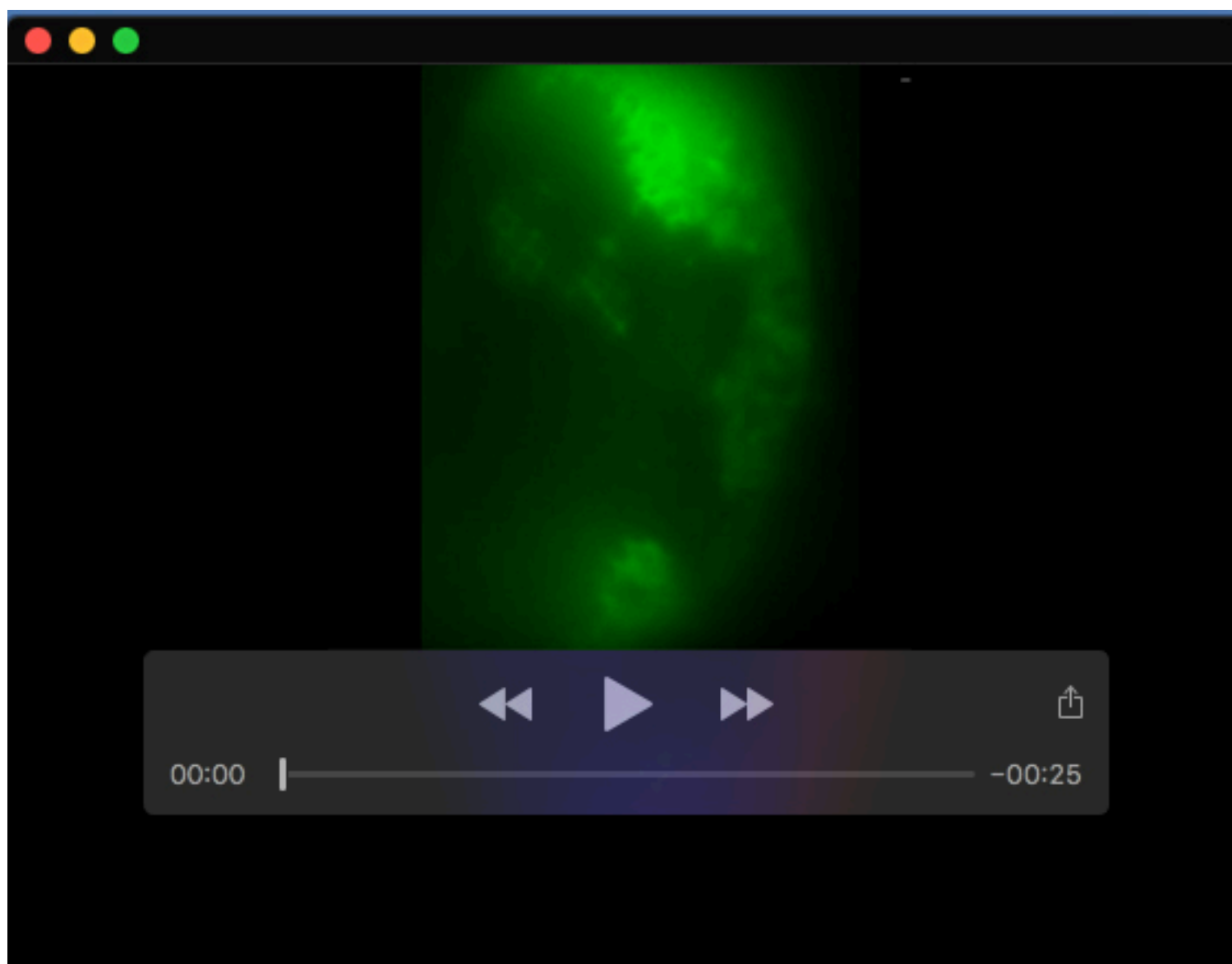
Movie 2. Young *IGMR>GCaMP6m/+* adult retina at a proximal plane (Fig. 3), showing Ca²⁺ waves in primary pigment cells.



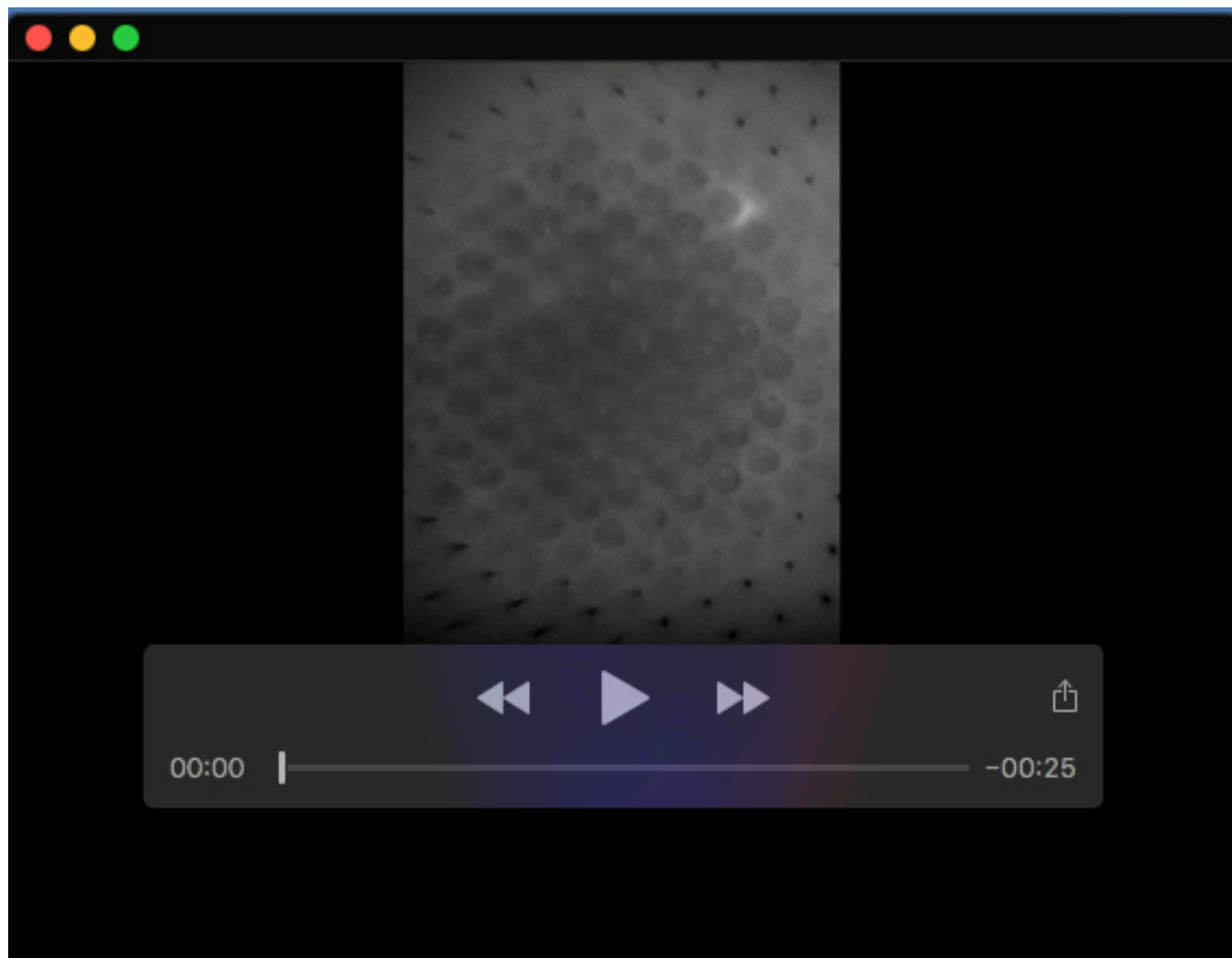
Movie 3. Young IGMR>GCaMP6m/+ adult retina at a proximal plane (Fig. S3), showing Ca²⁺ waves in primary pigment cells in the center and IOC waves in the periphery of the eye.



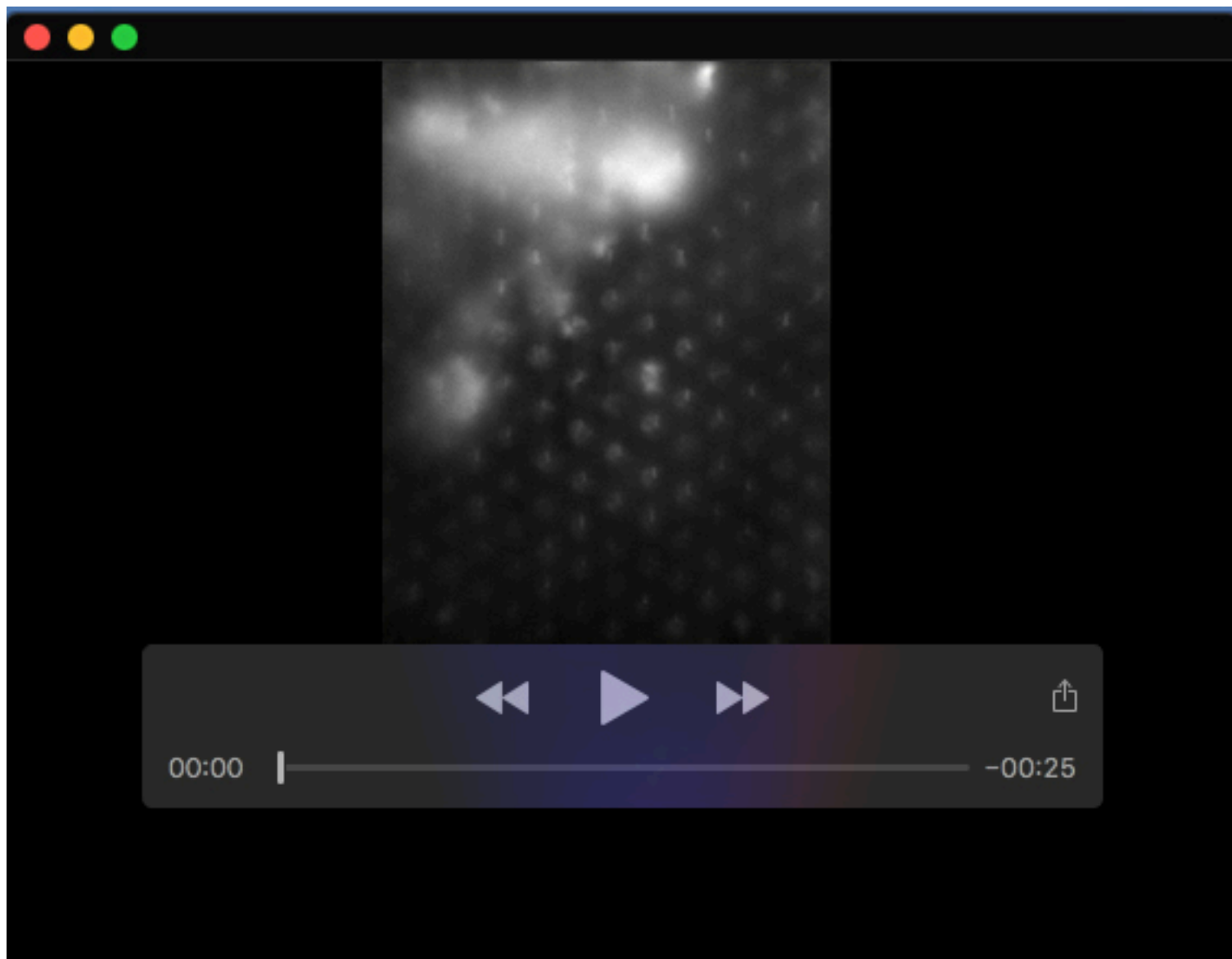
Movie 4. Young *IGMR>GCaMP6m/+* adult retina at a proximal plane (Fig. 4), showing Ca^{2+} activities in cone cells.



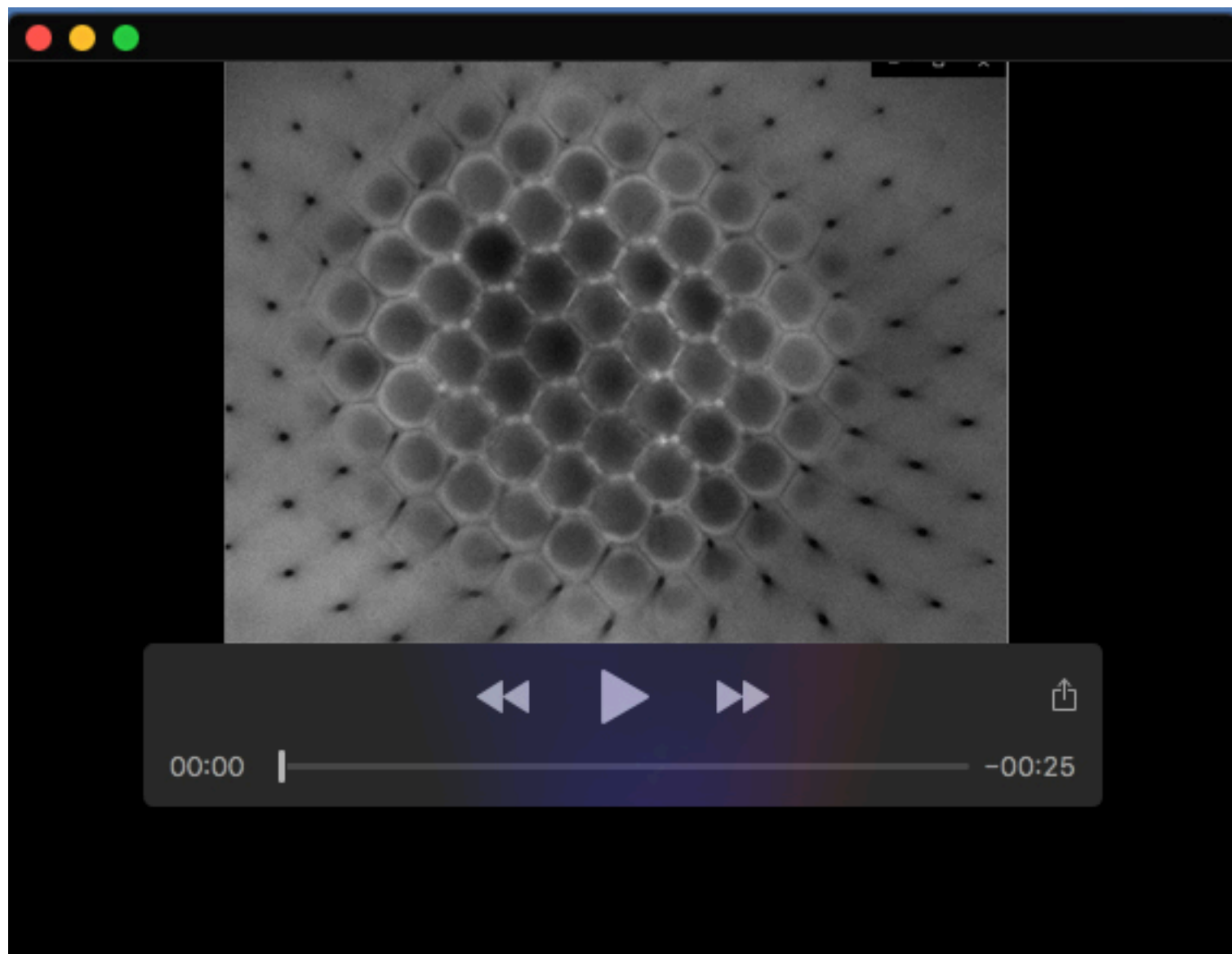
Movie 5. *ey>GCaMP6m/+* larval eye disc (Fig. S4). This time lapse was captured for a 10-minute duration.



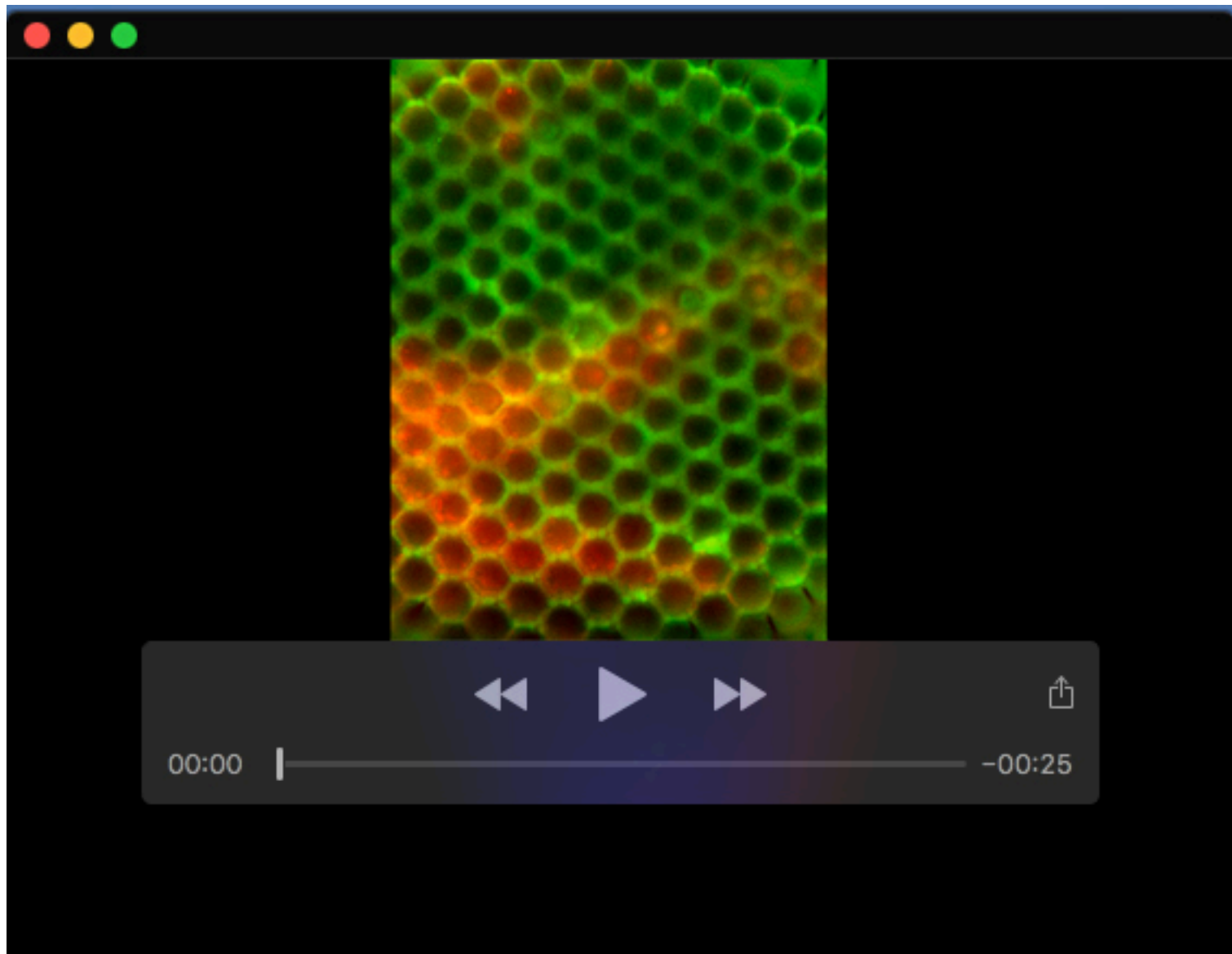
Movie 6. *IGMR>GCaMP6m/+* pupal retina at approximately P12 stage (Fig. 5).



Movie 7. The same *IGMR>GCaMP6m/+* pupal retina from Movie 6 imaged one day later (Fig. 5).



Movie 8. Young *norpA*^{36/Y}; *IGMR>GCaMP6m/+* adult retina at a distal plane (Fig 6).



Movie 9. Young *GMR>GCaMP6m/+* adult retina containing *IP3R*⁻ mutant patches (Fig. 6).